Neurobiology of Disease

Imbalance in Glucose Metabolism Regulates the Transition of Microglia from Homeostasis to Disease-Associated Microglia Stage 1

Yuxi Liu,[1] Witty Kwok,[1] Hyojung Yoon,[2] Jae Cheon Ryu,[1] Patrick Stevens,[3] Tara R. Hawkinson,[4,5] Cameron J. Shedlock,[4,5] Roberto A. Ribas,[4,5] Terrymar Medina,[4,5] Shannon B. Keohane,[4,5] Douglas Scharre,[6] Lei Bruschweiler-Li,[7] Rafael Bruschweiler,[7] Alban Gaultier,[8] Karl Obrietan,[2] Ramon C. Sun,[4,5] and Sung Ok Yoon[1]

[1]Department of Biological Chemistry and Pharmacology, The Ohio State University, Columbus, Ohio 43210, [2]Department of Neuroscience, The Ohio State University, Columbus, Ohio 43210, [3]Department of Biomedical Informatics, The Ohio State University, Columbus, Ohio 43210, [4]Department of Biochemistry and Molecular Biology, College of Medicine, University of Florida, Gainesville, Florida 32610, [5]Center for Advanced Spatial Biomolecule Research, University of Florida, Gainesville, Florida, 32610, [6]Department of Neurology, The Ohio State University, Columbus, Ohio 43210, [7]Department of Chemistry and Biochemistry, The Ohio State University, Columbus, Ohio 43210, and [8]Center for Brain Immunology and Glia, University of Virginia, Charlottesville, Virginia, 22908

Microglia undergo two-stage activation in neurodegenerative diseases, known as disease-associated microglia (DAM). TREM2 mediates the DAM2 stage transition, but what regulates the first DAM1 stage transition is unknown. We report that glucose dyshomeostasis inhibits DAM1 activation and PKM2 plays a role. As in tumors, PKM2 was aberrantly elevated in both male and female human AD brains, but unlike in tumors, it is expressed as active tetramers, as well as among TREM2$^+$ microglia surrounding plaques in 5XFAD male and female mice. snRNAseq analyses of microglia without *Pkm2* in 5XFAD mice revealed significant increases in DAM1 markers in a distinct metabolic cluster, which is enriched in genes for glucose metabolism, DAM1, and AD risk. 5XFAD mice incidentally exhibited a significant reduction in amyloid pathology without microglial *Pkm2*. Surprisingly, microglia in 5XFAD without *Pkm2* exhibited increases in glycolysis and spare respiratory capacity, which correlated with restoration of mitochondrial cristae alterations. In addition, in situ spatial metabolomics of plaque-bearing microglia revealed an increase in respiratory activity. These results together suggest that it is not only glycolytic but also respiratory inputs that are critical to the development of DAM signatures in 5XFAD mice.

Key words: **Alzheimer's disease; DAM genes; glycolysis; metabolism; microglia; PKM2**

Significance Statement

Although reduced glucose uptake in the brain has been recognized as one of the earliest pathological events that accompany Alzheimer's disease (AD), it has not been clear whether this was due to a brain-wide defect in glucose metabolism or a dysfunction in a particular cell type. Our data suggest that dysregulation of metabolic homeostasis in microglia is critical for global AD pathology in a mouse model. Upon restoring glucose metabolism in microglia genetically, AD pathology is attenuated with a concomitant increase in DAM genes, especially DAM1 genes. These results suggest that this increase in DAM gene expression is protective against AD pathology and glucose dyshomeostasis is a trigger to inhibit expression of protective DAM genes in AD.

Received Aug. 16, 2023; revised March 21, 2024; accepted March 23, 2024.

Author contributions: Y.L., R.C.S., and S.O.Y. designed research; Y.L., W.K., H.Y., J.C.R., T.R.H., C.J.S., R.A.R., T.M., S.B.K., and S.O.Y. performed research; Y.L., W.K., H.Y., P.S., T.R.H., R.C.S., and S.O.Y. analyzed data; D.S., L.B., R.B., and K.O. contributed unpublished reagents/analytic tools.

This work was supported by grants to S.O.Y. from NIH (R01AG055059, R01NS107456, R01DK120108), and grants from NIH to R.C.S. (5 R01AG066653, and 5 R01 AG078702). In addition, S10 OD026842 instrument grant and Genomics Shared Resource grant (NCI CCSG Grant P30CA016058) to Ohio State University.

The authors declare no competing financial interests.

Correspondence should be addressed to Sung Ok Yoon at sung.yoon@osumc.edu.

https://doi.org/10.1523/JNEUROSCI.1563-23.2024

Introduction

Brain hypometabolism is one of the pathological events that accompany Alzheimer's disease (AD) (Stanley et al., 2016). In particular, selective reduction in ^{18}F-fluorodeoxyglucose (FDG) uptake in vulnerable areas of the brain in presymptomatic *ApoE4* homozygous AD patients has been reported (Kennedy et al., 1995; Reiman et al., 1996), indicating that brain hypometabolism is one of the earliest dysfunctions in AD. More recently, large-scale proteomic analyses of >2,000 human AD brains and

~400 cerebrospinal fluid (CSF) samples identified the sugar metabolism module as the most significant module to be associated with AD pathology and cognitive decline out of 13 distinct modules that included the synapse/neuron module (Johnson et al., 2020). In this sugar metabolism module, several glycolytic gene products were included, such as glyceraldehyde-3-phosphate dehydrogenase (GAPDH), α-enolase (ENO1), pyruvate kinase muscle isoform (PKM), and lactate dehydrogenase b (LDHb), and of those, PKM and LDHb proteins were also detected in CSF samples. PKM and LDHb protein levels positively correlated with AD progression, highlighting the role of glucose metabolism in AD pathology. The major cell types represented in the sugar metabolism module are microglia and astrocytes, suggesting that the loss of control of glucose and carbohydrate metabolism in microglia and astrocytes plays a critical role in AD pathology.

Once taken up, glucose is metabolized through glycolysis and then oxidative phosphorylation via the TCA cycle to generate ATP. In metabolically active differentiated cells, oxidative phosphorylation dominates by virtue of generating higher levels of ATP than glycolysis per glucose unit (Vander Heiden et al., 2009; Van den Bossche et al., 2017). Actively proliferating cancer cells and immune cells on the other hand are known to undertake metabolic reprogramming in response to changes in metabolic demand or energy availability. A key molecule in this metabolic process is PKM2. PKM2 is the alternatively spliced isoform of PKM pre-mRNA, where PKM1 includes exon 9, while PKM2 includes exon 10 in a mutually exclusive manner (David et al., 2010; Chen et al., 2012). PKM2 is mainly expressed among proliferating cells in embryonic tissues, but its expression is often induced when cells resume proliferation during regeneration or tumor formation in the adult (Mazurek, 2011; Lunt et al., 2015). PKM2 is allosterically regulated by fructose-1,6-bisphosphate binding, switching between its inactive monomeric/dimeric form and its active tetrameric form, unlike PKM1 that exists as stable tetramers with high pyruvate kinase activity (Dayton et al., 2016). When induced in proliferating tumors, PKM2 is often tyrosine phosphorylated at Y105 in response to growth factor signaling (Hitosugi et al., 2009), resulting in inhibition of metabolically active tetramer formation. Such aberrant induction of enzymatically inactive PKM2 monomers/dimers in tumors leads to aerobic glycolysis with increased lactate production, termed the Warburg effect, where glycolytic metabolites are diverted from the TCA cycle to produce nucleotides, proteins, and lipids that are needed for generating daughter cells via proliferation at the expense of ATP production (Vander Heiden et al., 2009, 2011). In addition, PKM2 dimers can be translocated to the nucleus, activating transcription of glycolytic genes thereby regulating aerobic glycolysis (Yang et al., 2011; Gao et al., 2012).

Besides in tumors, PKM2 was shown to be induced in immune cells, such as macrophages and T cells, wherein metabolic pathways are known to regulate their phenotype and function in addition to providing energy (Van den Bossche et al., 2017; Geltink et al., 2018). For instance, as a dimeric form, nuclear PKM2 was shown to activate signal transducer and activator of transcription 3 (STAT3) to induce pro-inflammatory cytokines, such as IL-6, IL-1β, and IL-17 in T cells, in part by increased lactate production (Pucino et al., 2019; Angiari et al., 2020). In contrast, when PKM2 is stabilized as a tetrameric form pharmacologically with DASA-58 or TEPP-46, IL-17 production is reduced in T cells under inflammatory conditions (Angiari et al., 2020; Seki et al., 2020). These results suggest that activation of the glycolytic pathway is critical for maintaining pro-inflammatory macrophages, while anti-inflammatory macrophages employ oxidative phosphorylation instead.

Microglia belong to a myeloid lineage and are known to undergo metabolic changes in neurodegenerative diseases, for instance, via triggering receptor expressed on myeloid cells 2 (TREM2) (Kleinberger et al., 2017; Ulland et al., 2017; Parhizkar et al., 2023). PKM2 expression in microglia in vivo has been reported under neuropathological conditions (Romero-Ramirez et al., 2022; Li et al., 2023), including human AD cases and in 5XFAD mice (Pan et al., 2022). In particular, Pan et al. reported that PKM2 in microglia of 5XFAD mice promotes aerobic glycolysis by increasing lactate production, thereby modifying lactylation of histones, which in turn activates glycolytic genes (Pan et al., 2022). These actions presumably rely on monomeric/dimeric forms of PKM2 that favor aerobic glycolysis over oxidative phosphorylation producing lactate as in tumors. Here, we report that in addition to promoting aerobic glycolysis most likely as dimers as Pan et al. described (Pan et al., 2022), PKM2 also influences the respiratory capacity of microglia in 5XFAD mice as tetramers. A tetrameric form of PKM2 is highly expressed in brain tissues from human AD patients and 5XFAD mice. When PKM2 was activated with TEPP-46 to form tetramers in primary microglia, microglia responded by decreasing glycolysis and oxidative phosphorylation. Deleting *Pkm2* from microglia using the same Cx3cr1-CreERT2 line as Pan et al. in contrast increased both glycolytic capacity and maximal respiration. These results suggest that the metabolic effects of *Pkm2* deletion are not homogeneous in one pathway, but includes multiple distinct pathways, such as alteration in respiratory responses and glycolytic output, which together coordinate to control overall metabolic needs in microglia. In line with this notion, mitochondrial cristae in microglia in 5XFAD mice exhibit defects, which become restored with microglial deletion of *Pkm2*. In addition, metabolomics data from our in situ spatial metabolomics study illustrated that *Pkm2* deletion in microglia of 5XFAD mice led to increased mitochondrial respiratory activity with minor changes in glycolytic metabolites. In parallel with both glycolytic and respiratory metabolic changes induced by *Pkm2* deletion, expression of many DAM1 stage genes was increased in select metabolic cluster(s) of microglia upon *Pkm2* deletion. These data together suggest that the imbalance in glucose metabolism initiated by aberrant PKM2 activation as tetramers in microglia is a critical factor in regulating transition from homeostasis to DAM1 stage. Along with a recent report, in which deleting hexokinase 2 (HK2), the first enzyme in the glycolytic pathway from microglia, also caused a reduction in both glycolytic and respiratory capacity (Hu et al., 2022), our results suggest that perturbations in the glycolytic pathway will have an impact not only on glycolysis but also oxidative phosphorylation under neuropathological conditions.

Materials and Methods

Antibodies

Antibodies used for the study include; PKM1 (catalog #7067, RRID:AB_2715534), PKM2 (catalog #4053, RRID:AB_1904096), HK1 (catalog #2024, RRID:AB_2116996), HK2 (catalog #2867, RRID:AB_2232946), GAPDH (catalog #5174, RRID:AB_10622025), LDHA (catalog #2012, RRID:AB_2137173), PDH (catalog #3205, RRID:AB_2162926), PDHK1 (catalog #3820, RRID:AB_1904078), PFKFB3 (catalog #13123, RRID:AB_2617178), PSD95 (catalog #3450, RRID:AB_2292883), Aβ (NAB228, catalog #2450, RRID:AB_490857), p-AMPKα (catalog #2535, RRID:AB_331250), AMPKα (catalog #5831, RRID:AB_10622186), TREM2 (catalog #76765, RRID:AB_2799888), β-actin (catalog #3700,

RRID:AB_2242334), and APOE (catalog #49285 and catalog #68587) were from Cell Signaling Technology. PFKP (catalog #13389-1-AP, RRID:AB_2252278), and Aβ (6E10, catalog #SIG-39320-1000, RRID:AB_662798) were from Proteintech and Covance, respectively. Iba1 (catalog #ab5076-100, RRID:AB_2224402) from Abcam, GFAP (catalog #MAB360, RRID:AB_11212597) from Millipore, Amylo-Glo (catalog #TR-300-AG) from Biosensis, and vGlut1 and TREM2 for IHC from Drs Julia Kaltschmidt and Christian Haass, respectively. Secondary antibodies were from Thermo Fisher (catalog #A31572, RRID:AB_162543; S21381, RRID:AB_2307336; A11055, RRID:AB_2534102; SA1011; A11029, RRID:AB_2534088; A10525, RRID:AB_2534034) or from Jackson ImmunoResearch Labs (catalog #305-035-045, RRID:AB_2339403; 711-035-152, RRID:AB_10015282; 705-065-147, RRID:AB_2340397; 712-165-150, RRID:AB_2340666). Topro-3 was from Thermo Fisher (catalog #T3605).

Other reagents

Quantikine ELISA human amyloid β (aa 1–42) immunoassay kit (R&D Systems, catalog #DAB142), Lactate-Glo Assay kit (Promega, catalog #J5021), Adult Brain Dissociation Kit (Miltenyi, catalog #130-107-677), Cd11b/c conjugated beads for rat (Miltenyi, catalog #130-105-634), Cd11b conjugated beads for mouse (Miltenyi, catalog #130-093-634), DSS (Thermo Fisher, catalog #A39267), TRIzol Reagent (Invitrogen, catalog #15596-018), PowerUp SYBR Green Master Mix (Applied Biosystems, catalog #A25778), Protector RNase Inhibitor (Roche, catalog #03335399001), OneTaq RT-PCR kit (New England Biolabs, catalog #E5310S), SlowFade Diamond Antifade Mountant (Thermo Fisher, catalog #S36972), TEPP-46 (MedChemExpress, catalog #HY-18657), XF24 cell culture microplate (Agilent, catalog #100777-004), XFe24 FluxPak (Agilent, catalog #102340-100), XF Calibrant (Agilent, catalog #100840-000), XF basal media (Agilent, catalog #102353-100), 1 M glucose solution (Agilent, catalog #103577-100), 100 mM Pyruvate solution (Agilent, catalog #103578-100), 200 mM glutamine solution (Agilent, catalog #103579-100), 2-deoxyglucose (Cayman, catalog #14325), glucose (Sigma, catalog #G7528), oligomycin (Millipore, catalog #495455), FCCP (Cayman, catalog #15218), rotenone (Cayman, catalog #13995), MEM (Gibco, catalog #61100-061), DMEM (Gibco, catalog #12800-017), Fetal bovine serum (Gibco, catalog #10437-028), Penicillin and streptomycin (Gibco, catalog #15140-122), Trypsin (Gibco, catalog #15090-046), DNase I (Worthington, catalog #LS002147), 40 μm Flowmi Tip Strainer (Bel-Art, catalog #H13680-0040), all other chemicals were from Sigma.

Human tissue samples

Tissues from the frontal cortex were obtained through the UCSD Experimental Neuropath Laboratory (RRID:SCR_114906). The ages of AD and control cases ranged from 71 to 91 and 69 to 97 years, respectively. The Braak scores for AD cases were 6.2–6.3 and for control cases were 0.0–3.0.

Transgenic mice

All mice were obtained from Jackson Lab: 5XFAD (#34840, RRID:MMRRC_034840-JAX) (Oakley et al., 2006), Cx3cr1-CreERT2 (#021160, RRID:IMSR_JAX:021160) (Parkhurst et al., 2013), $PKM2^{fl/fl}$ (Israelsen et al., 2013) (#024048, RRID:IMSR_JAX:024048), and Cx3cr1-GFP (#005582, RRID:IMSR_JAX:005582) (Jung et al., 2000). 5XFAD from Jackson Lab in B6/SJL F1 hybrid background was made congenic by backcrossing 10 generations with C57/BL6. To generate microglial deletion of PKM2 in 5XFAD background, $5XFAD^{+/-}$:$Cx3cr1\text{-}CreERT2^{+/-}$:$PKM2^{fl/+}$ mice were bred with C57/BL6:$Cx3cr1\text{-}CreERT2^{-/-}$:$PKM2^{fl/+}$ mice to obtain the experimental $5XFAD^{+/-}$:$Cx3cr1\text{-}CreERT2^{+/-}$:$PKM2^{fl/fl}$ and the control $5XFAD^{+/-}$:$Cx3cr1\text{-}CreERT2^{+/-}$:$PKM2^{+/+}$ mice. For brevity, the experimental mice are designated as FAD:i-$PKM2^{M\Delta}$ and the control as FAD:i-$PKM2^{MC}$. PKM2 was deleted from microglia at 2 months via daily oral gavage for 5 d with 75 mg/kg of tamoxifen dissolved in 10% ethanol and 90% oil. All experimental mice were housed in an animal facility with ad libitum access to food and water on a 12/12 h light/dark cycle. All animal protocols were approved by the Institutional Animal Care and Use Committee (IACUC) at the Ohio State University. Both males and females were used at the same time throughout the project.

ELISA

Mice were transcardially perfused with ice-cold saline. The isolated brain hemispheres were homogenized with a Dounce homogenizer in 1 ml per 0.1 g tissue of Solution A containing 0.32 M sucrose, 10 mM HEPES (pH 7.4), 2 mM EDTA, supplemented with 1 mM sodium orthovanadate, 10 mM β-glycerophosphate, 10 μg/ml leupeptin, 1 μg/ml aprotinin, and 1 mM PMSF. Homogenates were supplemented with 1 ml per 0.1 g tissue of 0.2% diethylamine (DEA) in 50 mM NaCl and centrifuged at 100,000 G, 4°C for 1 h. The supernatant was neutralized with 1/10 volumes of 0.5 M Tris (pH 6.8) to obtain the soluble fraction. The pellet was resuspended in 100 μl of 70% formic acid and sonicated 3 times for 30 s. Then the mixture was neutralized with 15 volumes of 1.5 M Tris (pH 8.8) to obtain the insoluble fraction. Aβ42 levels in the soluble and insoluble fractions were measured using the Quantikine ELISA Human Amyloid β (aa1–42) Immunoassay kit (R&D Systems, catalog # DAB142) according to the manufacturer's instructions.

Amylo-Glo staining

To detect Aβ plaques in the mouse brains, Amylo-Glo staining was done according to the manufacturer's instructions (Biosensis catalog #TR-300-AG). Briefly, mouse brain sections were treated with 70% ethanol for 5 min, followed by water for 2 min. Then sections were incubated with 1× Amylo-Glo for 10 min and rinsed with saline for 5 min followed by water for 15 s. After that, sections were subjected to immunohistochemical analysis.

Lactate measurement. Rat primary microglia were treated with TEPP-46 (75 μM) for 1 h. Then the culture media were collected. Lactate levels were measured using the Lactate-Glo Assay kit (Promega, #J5021) according to the manufacturer's instructions.

Immunohistochemistry of mouse brain tissues

Mice were transcardially perfused with 3% paraformaldehyde in 0.1 M phosphate buffer (pH 7.2). The isolated brains were postfixed in the same buffer for 2 h at room temperature prior to cryoprotection in 20% sucrose in 0.1 M phosphate buffer at 4°C for 24 h. The brains were then sectioned at 30 μm on the coronal plane and collected as floating sections. For immunohistochemistry, sections containing the hippocampus and cortex (bregma −1.94 mm) were first blocked for 2 h at room temperature with 10% horse serum, 1% bovine serum albumin (BSA), and 0.3% Triton X-100 in 1× Tris-buffered saline (TBS), and incubated with primary antibodies in the incubation buffer containing 5% horse serum, 0.5% BSA, and 0.3% Triton X-100 in 1× TBS overnight. Antibody binding was detected by incubating sections with fluorescently labeled secondary antibodies for 2 h in the incubation buffer. After staining nuclei with Topro-3 (0.2 μM), sections were mounted in SlowFade Diamond Antifade Mountant (Thermo Fisher), and imaged either on Zeiss LSM 900 Airyscan two-point scanning confocal microscope (RRID:SCR_022263) or Andor revolution WD spinning disk confocal microscope. For quantification and analyses, FIJI software was utilized. For imaging and quantification of $vGlut1^+$ and $PSD95^+$ puncta, the spatial overlap between vGlut1 and PSD95 were measured using Synapse Counter, as described previously (Dzyubenko et al., 2016), in addition to analyzing whether the overlap was on the same plane through orthogonal views.

Western blotting

Primary microglia and fresh brain tissues were homogenized in lysis buffer containing 1% NP-40, 10% glycerol, 20 mM Tris (pH 8.0), 137 mM NaCl, 1 mM $MgCl_2$, 0.5 mM EDTA, 10 mM sodium pyrophosphate, supplemented with 1 mM sodium orthovanadate, 10 mM β-glycerophosphate, 10 μg/ml leupeptin, 1 μg/ml aprotinin, and 1 mM PMSF. Homogenates were rotated at 4°C for 15 min and centrifuged at 14,000 rpm, 4°C for 10 min, and supernatants were collected as lysates. Western blotting was done as previously described (Yoon et al., 2012).

Crosslinking of PKM2 proteins

Protein lysates were subjected to crosslinking as described (Palsson-McDermott et al., 2015). Briefly, lysates from primary microglia and brain tissues were incubated with 0.5 mM DSS at room temperature

for 30 min. The reaction was quenched with 50 mM Tris (pH 7.5) at room temperature for 15 min. Crosslinked lysates were resolved on 5–20% polyacrylamide gradient gels and subjected to Western blotting analyses using PKM2 antibody.

Two-photon live imaging of microglial recruitment in vivo

Cx3cr1-GFP mice were subjected to surgery to create a cranial window when they were 3–4 months old. To reduce inflammation and pain, ibuprofen (5 mg/kg in drinking water) and buprenorphine (0.05 mg/kg, SC) were administered to mice for a day before the surgery. In addition, on the day of the surgery, carprofen (5 mg/kg, SC) was administered to reduce edema and inflammation.

Mice were anesthetized under an isoflurane/oxygen mixture (5% for induction and 2% for maintenance), and the isoflurane flow was controlled by scavenging vaporizer (catalog #: 72–6468, RRID: SCR_018956, Harvard Apparatus). Throughout the surgery, body temperature was maintained with a heating pad, and an eye ointment was applied to prevent dryness and provide protection from other solutions used during the surgery. Animals were placed onto the stereotactic table (Cartesian Research) and secured into position. The fur was removed to expose the scalp which was then disinfected three times using independent swabs with 70% EtOH and betadine. An incision was made to expose skull and periosteum was removed. A circular craniotomy of about 3 mm was made with high-speed drill at the position of AP: −2.00 mm, ML: 1.7 mm. No.1 coverglass (Harvard Apparatus) was glued above the craniotomy with Vetbond (3 M) and dental cement. A custom-made plastic head bar was secured to the skull with the dental cement to immobilize the head during imaging. Ibuprofen was provided in drinking water for 2–3 d postoperation. Mice were allowed to recover from the operation for a minimum of 2 weeks prior to imaging.

For two-photon laser stimulation and in vivo imaging, mice with cranial windows were treated daily for 4 d via oral gavage with either vehicle (0.5% carboxymethyl cellulose, 0.1% Tween 80) or TEPP-46 at 50 mg/kg. On the fifth day, mice were anesthetized with an isoflurane/oxygen mixture (5% induction and 1.5% maintenance) and placed onto a stainless-steel frame with the head immobilized. The stainless-steel frame was then secured to a motorized stage using a FVMPE-RS multiphoton microscope system (Olympus Corporation). With a 25× water immersion objective (catalog #: XLPLN25XWMP2, Olympus), blood vessels on the cortical surface of the brain were visualized through the cranial window. Cortical cells ∼50 µm below the surface was imaged with a Ti: Sapphire laser (Chameleon Vision II, Coherent). The region of interest (ROI) circle was drawn and irradiated with a 700 nm laser at 100% power for 1 s. The time series of images were acquired every 1 min for 1 h using a GaAsP photomultiplier tube through a yellow dichroic filter (FV30-FCY, Olympus) at a 920 nm wavelength.

Images were analyzed as described in Etienne et al. (2019) with open-source analysis platform ImageJ and Icy (de Chaumont et al., 2012). Images were first processed with MultiStackReg plugin in ImageJ (align; transformation, rigid body) for correction of drifts. The modified images were then imported into Icy and a 35 µm circle was drawn, centered on the lesion site. The signal was measured as mean intensity with ROI intensity evolution plugin over time and measured for 1 h. The measured value was then exported as .XLS file and normalized with the equation: $R(t) = (R_{\text{inner}}\ (t) - R_{\text{inner}}\ (0))/R_{\text{outer}}\ (0)$ according to (Davalos et al., 2005). Each value from the time points was normalized by the mean of baseline value. Normalized value was statistically tested with paired *t* test (two-tailed, $p < 0.0001$) using GraphPad Prism (GraphPad software).

Primary microglia cultures

Brains from Sprague Dawley rat pups at postnatal day 1–2 were isolated and dissected to obtain cortices and hippocampi in ice-cold 120 mM NaCl, 2.5 mM KCl, 10 mM $NaHCO_3$, 1 mM NaH_2PO_4, 20 mM glucose, and 20 mM HEPES. Following 20 min digestion at 37°C with 0.25% trypsin and 2.5 mg/ml DNase I, tissues were triturated with a fire-polished glass pipette in minimum essential media (MEM) supplemented with 10% fetal bovine serum (FBS) and 1% penicillin and streptomycin (P/S). Single cells from two brains were plated on one poly-D-Lysine coated T-75 flask, and the culture medium was changed once every third day and thereafter. On days 10–11 in vitro (DIV10–11), microglia were isolated by a shake-off method using a shaker at 150 rpm, 37°C for 4 h. Isolated microglia were subsequently immunopurified using CD11b/c antibody conjugated beads (Miltenyi, catalog # 130–105-634, RRID:AB_2783886) and plated at $0.3–0.8 \times 10^6$ cells/ml on PDL-coated dishes or coverglasses in Dulbecco's modified Eagle's medium (DMEM) with 10%FBS and 1%P/S. Purified microglia were typically cultured for 3–4 d (37°C, 5%CO_2) prior to experimentation.

Metabolic stress treatment

Rat primary microglia were plated in 6- or 12-well plates at a density of $0.7–0.8 \times 10^6$/well or $0.3–0.4 \times 10^6$/well, respectively. Two to three days after plating, microglia were treated with TEPP-46 (75 µM), 2-DG (1 mM), IACS-010759 (100 nM), dichloroacetate (DCA, 5 mM) for 24 h or indicated time points.

MALDI-MSI sample preparation and data export

Slides were prepared as previously described, (Hao et al., 2021), in brief, High-performance liquid chromatography (HPLC)-methanol, HPLC-grade water and N-(1-Naphthyl)ethylenediamine dihydrochloride (NEDC) matrix were obtained from Sigma-Aldrich. Tissue was slow frozen over a bath of dry-ice cold 2-methylbutane for 7 min prior to storage in −80°C until cutting on slides. Brains were cut on a Lecia CM1860 cryostat at 10 µm onto positively charged glass slides and stored in the −80°C until the day of sample preparation. On day of run, the slides were removed from the freezer and placed in a desiccator for 1 h. Slides were immediately sprayed with 14 passes of 7 mg/ml NEDC matrix in 70% methanol, applied at 0.06 ml/min with a 3 mm offset and a velocity of 1,200 mm/min at 30°C and 10psi using the M5 Sprayer with a heated tray of 50°C. Slides were used immediately or stored in a desiccator until use. For the detection of metabolites, a Bruker timsTOF QTOF high-definition mass spectrometer was used. The laser was operating at 10,000 Hz with 60% laser energy, with 300 laser shots per pixel and spot size of 50 µm at X and Y coordinates of 50 µm with mass range set at 50–2,000 m/z in negative mode. Data acquisition spectrums were uploaded to Scils Software (Bruker Corporation) for the generation of small molecules. Regions of interest (ROIs) were drawn around brain regions based on the Allen Brain Atlas and exported using the SCILs lab API as tabular format. Pixel to pixel information and statistical analysis are performed using GraphPad Prism9 (RRID:SCR_002798). The data are represented as relative abundance is the area under the curve for each mass spec peak and normalized to total ion current.

Microglia isolation from adult mouse brain for snRNAseq and protein analyses

Mice were transcardially perfused with ice-cold saline. Brains were isolated and dissociated using the Adult Brain Dissociation Kit (Miltenyi, catalog #130-107-677). After dissociation, the cells were triturated with a fire-polished glass pipette in HEBSS solution (120 mM NaCl, 2.5 mM KCl, 10 mM $NaHCO_3$, 1 mM NaH_2PO_4, 20 mM glucose, 20 mM HEPES) and filtered through a 40 µm cell strainer. The cell suspension was then centrifuged at 300 rcf for 5 min at 4°C. The cell pellet was resuspended with 37% Percoll and subjected to a Percoll gradient (70%, 37%, 30%, 0%) at 4°C, and was centrifuged for 40 min at 300 g (Lee and Tansey, 2013). Microglia were collected at the 70–37% interphase, washed with 12 ml HEBSS and then immuno-purified using CD11b antibody-conjugated microbeads (Miltenyi, catalog #130-093-634). For Western blotting, proteins were extracted with lysis buffer (Harrington et al., 2002), and snap frozen in liquid N2 and stored at −80°C until analyses. For single nucleus RNA sequencing, the purified microglia were resuspended with 10% DMSO/90% fetal bovine serum (FBS) and cryopreserved in liquid nitrogen until all mice were harvested.

Single nucleus RNA sequencing of microglia

Single nuclei were isolated from microglial cell suspensions according to the 10× Genomics Sample Preparation Demonstrated Protocol. Briefly, cell suspension was centrifuged at 300 rcf for 5 min, and the cell pellet was resuspended with 1 ml Lysis Buffer (10 mM Tris-HCl, 10 mM NaCl, 3 mM $MgCl_2$, and 0.1% NP40 in nuclease-free water) using a wide-

bore pipette tip. Then the cells were lysed on ice for 5 min and centrifuged at 500 rcf for 5 min at 4°C. The nuclei pellet was washed with 1 ml Nuclei Wash and Resuspension Buffer (1× PBS with 2% BSA and 0.2 U/μl RNase inhibitor) for 2 times using a regular-bore pipette tip. After the second wash, the nuclei pellet was resuspended with an appropriate volume of Nuclei Wash and Resuspension Buffer to achieve a concentration of 1,000 nuclei/μl and filtered through a 40 μm Flowmi Tip Strainer. The nuclei concentration was determined using a hemocytometer and adjusted to 1,000 nuclei/μl. Then the nuclei were then subjected to chip loading immediately using the 10× Genomics Chromium Next GEM Single Cell 3′ Reagent kits v3.1 at Ohio State University Genomics Shared Resource.

Single-nucleus RNA-Seq data processing and alignment

Sequenced single cell reads in FASTQ format were aligned to a reference transcriptome using the GRCm38 (mm10) genome (downloaded March 2021 refdata-gex-mm10-2020-A build from 10× Genomics website) using 10× Genomics Cell Ranger software (Cell Ranger 6.0.0 (Zheng et al., 2017)) based on default parameters with include-introns function. Output files from Cell Ranger count was analyzed using Seurat 4.0.4 (Hao et al., 2021). Briefly, QC-filtered cells were further selected based on RNA content thresholds: greater than 200; less than 4,000 unique expressed genes (nFeature_RNA) and mitochondrial gene content less than 20%. Preprocessed data from the 6 samples were integrated using the standard processing with Seurat. Data were normalized using log1p via the NormalizeData function (Hao et al., 2021). Variable features were found with the FindVariableFeatures function (2,000 features). After scaling and PCA normalization with default parameters, cells were partitioned into clusters using Seurat functions FindNeighbors and FindClusters functions (dimensions = 20, res = 0.2) with the Louvain algorithm. The identified clusters were then visualized using Uniform Manifold Approximation and Projection (UMAP) embeddings (dimensions = 20).

Feature Plots were generated using Seurat function FeaturePlot using the RNA assay. The module score was calculated from specified genes using the Seurat-implemented function AddModuleScore and generated using the FeaturePlot function as described (Hao et al., 2021). The module score is calculated by the average expression levels of each cluster at the single cell level subtracted by the aggregated expression of random control feature sets (200 by default). Cluster based differential expression was performed using the FindMarkers Seurat function using the RNA assay or normalized RNA data. Volcano plots were generated using the EnhancedVolcano [https://github.com/kevinblighe/EnhancedVolcano] R function based on normalized RNA assay data from the NormalizeData function.

Averaged expression matrix from each cluster was exported from Seurat using the AverageExpression function. Gene expression values were normalized using a row-based *z*-score calculation function were plotted using pheatmap function (Gu et al., 2016).

Volcano plot: Raw RNA expression data were normalized using NormalizeData function with default settings. This converts the expression values to natural log transformed using log1p. Differential expression of all microglia clusters (0,1,2,3,4,6) was performed between conditions using FindMarkers (only.pos = FALSE, min.pct = 0.15, logfc.-threshold = 0.15). A total of 484 significant genes were found. Volcano plots were generated using the EnhancedVolcano [https://github.com/kevinblighe/EnhancedVolcano].

Pathway enrichment analysis for microglia clusters was performed using Ingenuity Pathway Analysis (IPA) (Kramer et al., 2014). Raw data for IPA analysis was found using Seurat implemented function FindMarkers (only.pos = FALSE, min.pct = 0.15, logfc.threshold = 0.15) from each cluster/condition tested against all other cells. Differential expression output was analyzed in IPA core analysis using Expr log Ratio (confidence = experientially observed, species = Mouse, Tissue & cells lines = Nervous system and all Macrophages, stringent filtering on molecules and relationships). Likely activation states of biological functions were inferred based on comparison with a model that assigns random regulation. IPA *p*-value was calculated with the Fischer's exact test, reflects the likelihood that the association between a set of genes in dataset compared to IPA datasets. Based on QIAGEN metrics, IPA pathway *z*-score of greater or equal to positive 2 is considered activated, while a score less than or equal to negative 2 is considered an inhibited pathway. Ratio is the number of genes from the list that maps to the pathway divided by the total number of genes that map to the same pathway. Canonical Pathway and Upstream Regulator figures were generated using ggplot2 dotplot function [https://ggplot2.tidyverse.org/].

Cell-cell communication analysis was performed using CellChat (Jin et al., 2021) after clusters were labeled. Standard preprocessing steps were performed using the CellChatDB.mouse dataset. Analysis was performed independently between wild type (WT) and knock-out cells after removing nonmyeloid cells of interest and splitting the integrated dataset using Seurat SplitObject function. CellChat WT and knock-out objects were merged using merge CellChat function. Basic comparison analysis was used to generate figures. Figures were generated using default settings for each function.

Measurement and quantification of ECAR and OCR of rat and mouse microglia

Extracellular acidification rate (ECAR) and oxygen consumption rate (OCR) were measured using a Seahorse XFe24 analyzer (RRID: SCR_019539, Agilent). Rat primary microglia were immuno-purified from the mixed glia cultures isolated from P1-2 rats, and plated at 50,000–60,000 cells/well on an XF24 cell culture microplate that was precoated with 0.1 mg/ml PDL, and cultured for 3–4 d. The cartridge was hydrated in XF Calibrant buffer overnight in a CO_2-free 37°C incubator. On the day of the assay, the assay medium for ECAR (XF base medium with 4 mM glutamine) and OCR (XF base medium with 25 mM glucose, 1 mM pyruvate and 4 mM glutamine) were prepared freshly. To induce glycolytic and respiratory stress, glucose (10 mM), 2-deoxy-D-glucose (2-DG, 50 mM), oligomycin (1 μM), FCCP (0.5 μM) and rotenone (0.5 μM) /antimycin A (0.5 μM) were prepared as 10× solutions in respective assay media according to the Agilent's instructions.

For ECAR and OCR measurement on adult mouse microglia, the control FAD:i-PKM2^{MC} and experimental FAD:i-PKM2$^{M\Delta}$ mice were treated daily with 75 mg/kg of tamoxifen dissolved in 10% ethanol and 90% oil for 5 d via oral gavage at 1 month old. Two weeks after the last tamoxifen dosing, mouse brains were isolated and dissociated using the Adult Brain Dissociation Kit (Miltenyi, catalog #130-107-677) according to the manufacturer's instructions. Microglia were immuno-purified using CD11b antibody-conjugated microbeads (Miltenyi, catalog #130-093-634), plated at 60,000 cells/well on an XF24 cell culture microplate that was precoated with 0.1 mg/ml PDL, and cultured for 7 d in DMEM supplemented with 10%FBS, 1%P/S, 50 ng/ml granulocyte-macrophage colony-stimulating factor (GM-CSF), and 100 ng/ml macrophage colony-stimulating factor (M-CSF). One day before the Seahorse experiment, the cartridge was hydrated in XF Calibrant buffer overnight in a CO_2-free 37°C incubator. The assay medium (XF base medium with 4 mM glutamine) was prepared freshly on the day of the assay. Glucose (10 mM), 2-DG (50 mM), oligomycin (1 μM), FCCP (1.5 μM) and rotenone (0.5 μM) /antimycin A (0.5 μM) were prepared as 10× solutions in assay medium and added to the cell cultures to induce glycolytic and respiratory stress during the Seahorse experiment.

Transmission electron microscopy

Control FAD:i-PKM2^{MC} and experimental FAD:i-PKM2$^{M\Delta}$ mice were treated daily with 75 mg/kg of tamoxifen dissolved in 10% ethanol and 90% oil for 5 d via oral gavage at 2 months old. At 4 months, mice were transcardially perfused with ice-cold saline. Brains were isolated and dissociated using the Adult Brain Dissociation Kit (Miltenyi, catalog #130-107-677) according to the manufacturer's instructions. Microglia were immuno-purified using CD11b antibody-conjugated microbeads (Miltenyi, catalog #130-093-634). Freshly isolated microglia were immediately fixed in 2% paraformaldehyde/2.5% glutaraldehyde in 0.1 M sodium cacodylate buffer (pH 7.2) at room temperature for 1 h, and embedded in 2% agarose for TEM processing. Samples were postfixed with 1% osmium tetroxide and then en bloc stained with 1% aqueous uranyl acetate, dehydrated in a graded series of ethanol, and embedded in Eponate 12 epoxy resin (Ted Pella Inc.). Ultrathin sections were cut

Table 1. Primers for qPCR

Name	Forward primers	Reverse primers
Mouse Gapdh	AGCTTGTCATCAACGGGAAG	TTTGATGTTAGTGGGGTCTCG
Mouse Actb	GGCTGTATTCCCCTCCATCG	CCAGTTGGTAACAATGCCATGT
Mouse P2ry12	ATGGATATGCCTGGTGTCAACA	AGCAATGGGAAGAGAACCTGG
Mouse Cx3cr1	GAGTATGACGATTCTGCTGAGG	CAGACCGAACGTGAAGACGAG
Mouse Apoe	TGTTTCGGAAGGAGCTGACT	TGTGTGACTTGGGAGCTCTG
Mouse Trem2	AGGGCCCATGCCAGCGTGTGGT	CCAGAGATCTCCAGCATC
Mouse Tyrobp	GAGTGACACTTTCCCAAGATGC	CCTTGACCTCGGGAGACCA
Mouse Cstb	AGGTGAAGTCCCAGCTTGAAT	GTCTGATAGGAAGACAGGGTCA
Mouse Timp2	TCAGAGCCAAAGCAGTGAGC	GCCGTGTAGATAAACTCGATGTC
Mouse Cd33	CCGCTGTTCTTGCTGTGTG	AAGTGAGCTTAATGGAGGGGTA
Mouse Clu	CGAAGATGCTCAACACCTCA	TGTGATGGGGTCAGAGTCAA
Mouse Adam10	AGCAACATCTGGGGACAAAC	TTGCACTGGTCACTGTAGCC
Mouse Mef2c	CGGTGTCGTCAGTTGTATGG	TGCAGTAGATATGCGGCTTG
Mouse Sorl1	CCTGTCGCGTTTTTCTTAGC	TTCTGGCAATGCACTTCTTG
Rat Gapdh	GTATTGGGCGCCTGGTCACC	CGCTCCTGGAAGATGGTGATGG
Rat Trem2	AAGATGCTGGAGACCTCTGG	GGATGCTGGCTGTAAGAAGC
Rat Apoe	CTGGTTCGAGCCGCTAGTG	CCTGTATCTTCTCCATTAGGTTTGC

with a Leica EM UC6 ultramicrotome (Leica microsystems, EM FC7). Images were acquired with an FEI Tecnai G2 Spirit BioTwin transmission electron microscope (Thermo Fisher Scientific), and a Macrofire (Optronics, Inc.) digital camera and AMT image capture software. The length and area of mitochondrial cristae were measured and quantified with ImageJ.

Quantitative PCR

Total RNA was isolated from primary microglia and fresh mouse brain tissues using TRIzol Reagent according to the user guide. Equal amounts of total RNA (0.5–1 μg) were reverse transcribed using the OneTaq RT-PCR kit (New England Biolabs, catalog #E5310). Quantitative PCR (qPCR) was performed using PowerUp SYBR Green Master Mix (Applied Biosystems, catalog #100029284) and a QuantStudio 3 Real-Time PCR Instrument (Applied Biosystems). Primers used for qPCR are listed in Table 1. The relative mRNA levels of target genes were calculated using the ΔΔCt method, and Gapdh was selected as the endogenous control.

Experimental design and statistical analysis

Statistical analyses were performed using GraphPad Prism v9.3.0 (RRID: SCR_002798). The data are expressed as mean ± SEM. The significance between different experimental groups was tested by paired or unpaired Student's *t* test as indicated in the figure legends. When experimental groups include their own biological replicates, they are indicated. The *p*-values that were less than 0.05 were presented in the figures.

Results

Aberrant activation of PKM2 in Alzheimer's disease

As the first step to address a possible metabolic effect on AD pathology, we examined whether there are differences in glycolytic enzyme expression between WT control and 5XFAD mice. The protein expression of most enzymes did not show any changes, except for hexokinase 2 (HK2), the platelet isoform of phosphofructokinase (PFKP), and PKM2 (Fig. 1*A–D*). PKM2 in particular was present mainly as active tetramers in the brain, and its levels were increased in 5XFAD mice (Fig. 1*C,D*). Expression of its alternative isoform, PKM1, on the other hand showed no difference between the control and 5XFAD mice. This is in agreement with a recent paper where they showed an increase in PKM2 in 5XFAD mice, although they only tested for total PKM2 without distinguishing the active tetramers from inactive monomers and dimers (Pan et al., 2022). Similar increases in PKM2 tetramers and monomers but not PKM1 were detected when we analyzed human frontocortical lysates from AD cases compared to age matched controls (Fig. 1*E,F*).

We next sought to determine which cell types in the brain express PKM2 by performing immunohistochemistry on 5XFAD and control mouse brain sections at 4–5 months. In the WT mouse brain, PKM2 immunoreactivity was detectable at a very low level in Iba1$^+$ microglia and GFAP$^+$ astrocytes throughout different regions of the brain. In 5XFAD mice on the other hand, its expression increased dramatically, especially among Iba1$^+$ microglia that were associated with Amylo-Glo-labeled Aβ plaques (Fig. 2*A,B*). These PKM2$^+$ microglia near amyloid plaques also expressed high levels of TREM2, with expression of PKM2 and TREM2 colocalizing completely (Fig. 2*C,D*). Since TREM2 is known to regulate metabolic homeostasis in microglia (Ulland et al., 2017) and pyruvate kinase (PK) is a key enzyme that determines glycolytic activity, the complete colocalization of PKM2 and TREM2 expression in plaque-associated microglia may suggest a critical role of metabolic balance in TREM2-mediated function in microglia.

Microglial recruitment to amyloid plaques has been shown to be influenced by TREM2 (Wang et al., 2015; Parhizkar et al., 2019) and the microglia's energy status (Ulland et al., 2017; Baik et al., 2019). Since PKM2 is expressed in TREM2$^+$ microglia surrounding plaques, we asked whether activating PKM2 among microglia would influence chemotactic migration of microglia to an injury site. To address this question, PKM2 was activated with TEPP-46, a CNS penetrable PKM2-specific activator (Anastasiou et al., 2012; Angiari et al., 2020; Seki et al., 2020) in Cx3cr1-GFP mice, in which migration patterns of GFP$^+$ microglia toward injury site can be followed in vivo using two-photon microscopy. Our experimental scheme is depicted in Figure 3*A*: After 2 weeks of recovery from surgery, mice were treated once a day with TEPP-46 or vehicle for 4 d. two-photon microscopy was conducted on the following fifth day. In vehicle-treated control mice, GFP$^+$ microglia were rapidly recruited to the injury site reaching a peak in 45–60 min, while their migration was significantly slower and did not reach the peak in 60 min in TEPP-46 treated mice (Fig. 3*B,C*). These results are somewhat similar to those of a report where systemic delivery of 2-deoxyglucose (2-DG) completely blocked microglial migration for the entire 60 min in the same Cx3cr1-GFP mice (Baik et al., 2019). The authors concluded that it was mainly due to 2-DG inhibiting glycolysis. We thus tested whether our TEPP-46 treatment plan was indeed effective in inducing tetramerization of PKM2 by isolating Cd11b$^+$ microglia and measuring the extent of PKM2 tetramerization as in Figure. 1. A 4 d dosing of TEPP-46 was sufficient to induce PKM2 tetramerization in microglia compared to the vehicle control (Fig. 3*D*), which we interpret as suggesting that PKM2 must have influenced glycolysis and/or oxidative phosphorylation in TEPP-46 treated mice. It should also be noted that 2-DG is known to block both glycolysis and oxidative phosphorylation (Wick et al., 1957; Wang et al., 2018).

Baik et al. (2019) has also shown that Cx3cr1-GFP$^+$ microglial motility was significantly reduced in 5XFAD mouse background compared to the WT when lesioned with laser. Since TEPP-46 treatment increased tetramerization of PKM2 efficiently, and 5XFAD mice express high levels of PKM2 tetramers in microglia at 6–8 months of age (Figs. 1*C*, 2*C*), it could be concluded that the attenuated motility of Cx3cr1-GFP$^+$ microglia in 5XFAD mice was in part attributed to PKM2 tetramers.

To further investigate the effects of PKM2 activation on metabolism, we measured the effects of TEPP-46 on microglia bioenergetics using Seahorse analyses of primary rat microglia with and without TEPP-46. A 4 h pretreatment with TEPP-46

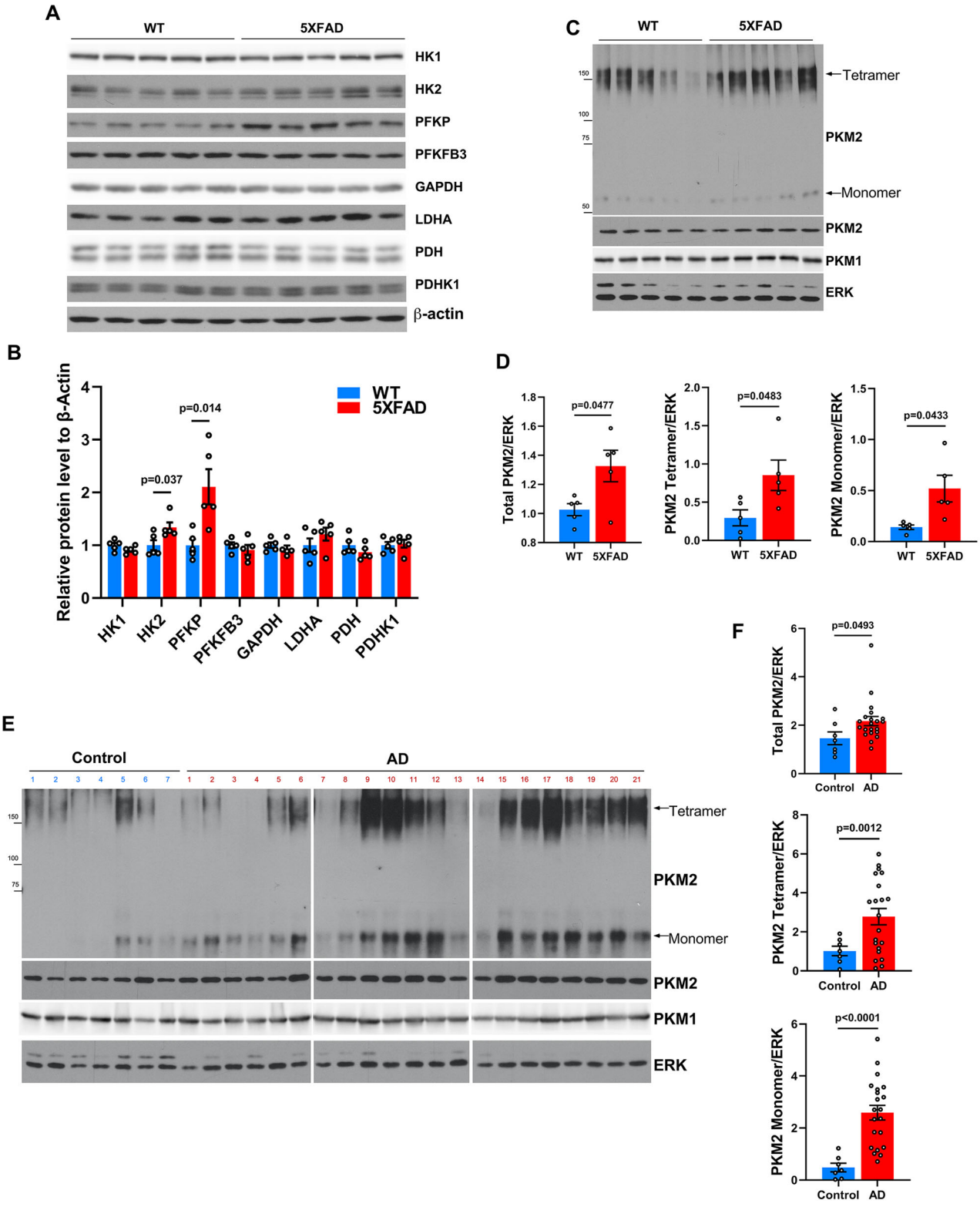

Figure 1. Aberrant activation of PKM2 in Alzheimer's disease. ***A***, Changes in glycolytic gene expression in the brains of 5XFAD mice. HK1, hexokinase 1; HK2, hexokinase 2; PFKP, phosphofructokinase, platelet; PFKFB3, 6-phosphofructo-2-kinase/fructose-2,6-biphosphatase 3; GAPDH, glyceraldehyde-3-phosphate dehydrogenase; LDHA, lactate dehydrogenase a; PDH, pyruvate dehydrogenase; PDHK1, pyruvate dehydrogenase kinase 1. ***B***, Quantification of the blots in (***A***) ($n = 5$, all M mice for each genotype). ***C***, PKM2 Western blot of protein lysates obtained from 6-month-old 5XFAD mice following DSS crosslinking. Control blots of PKM1 and ERK are also shown along with total PKM2 without crosslinking. ***D***, Quantification of total, active tetrameric, and inactive monomeric PKM2 in (***C***) ($n = 5$, all F mice for each genotype). ***E***, PKM2 Western blot of protein lysates obtained from frontal cortices of human AD and control subjects following DSS crosslinking. Control blots of PKM1 and ERK are also shown along with total PKM2 without crosslinking. ***F***, Quantification of total, active tetrameric, and inactive monomeric PKM2 in (***E***). ($n = 7$, 4 M + 3 F, control and $n = 21$, 10 M + 11 F, human AD subjects). Data are expressed as mean ± SEM. Unpaired Student's *t* tests were used in (***B, D, F***).

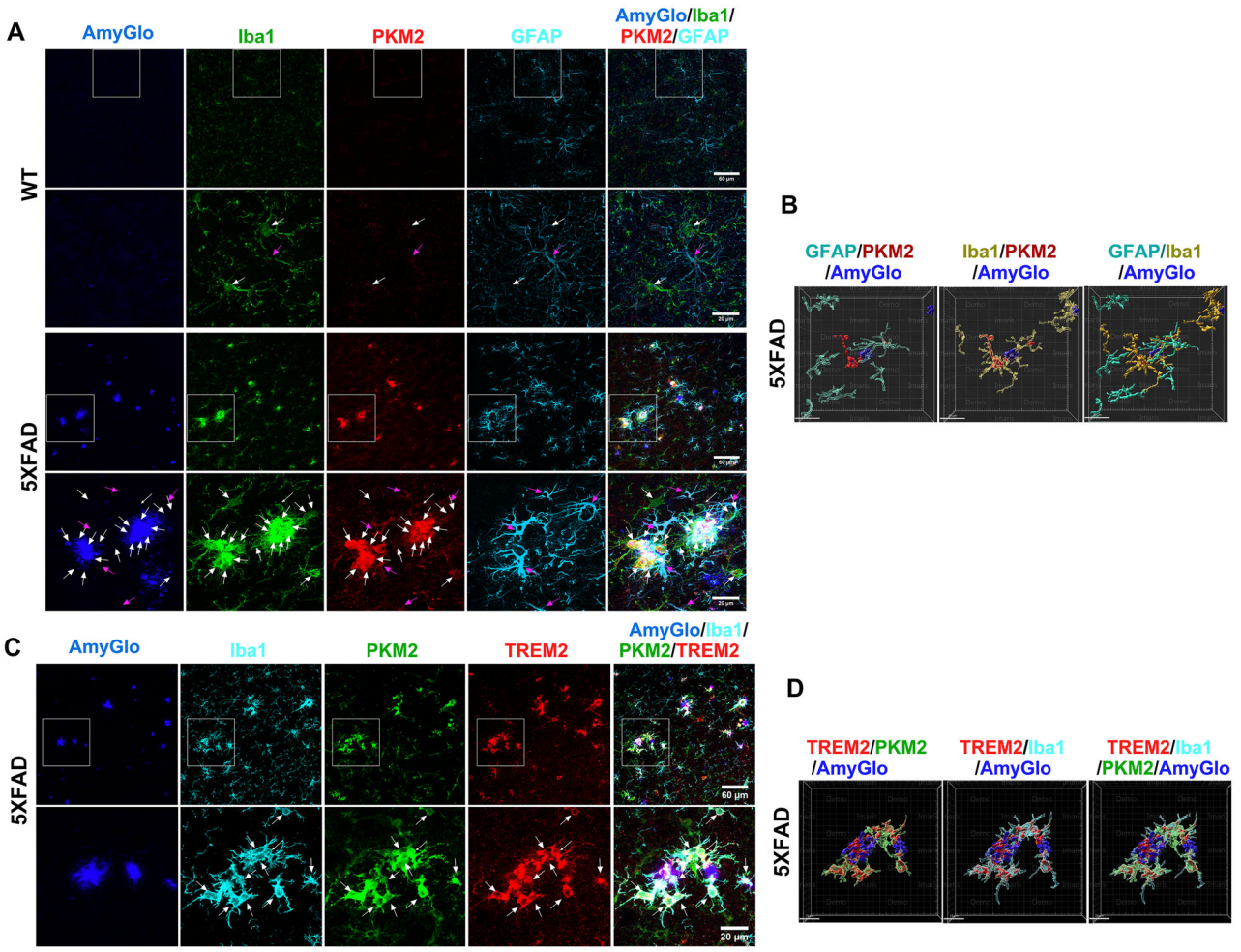

Figure 2. Upregulation of PKM2 in microglia in 5XFAD mice. ***A***, Representative images showing PKM2 expression in WT and 5XFAD mice at 4–5 months. PKM2 expression is selectively increased among Iba1$^+$ microglia that associate with plaques, and not in GFAP$^+$ astrocytes in 5XFAD mice. Note that pink arrows mark GFAP$^+$, while white arrows mark Iba1$^+$ cells. (n = 5, 2 M + 3 F, for WT and n = 5, 3 M + 2 F, for 5XFAD mice) ***B***, Imaris 3D reconstruction images showing colocalization of PKM2 with Iba1$^+$ microglia but not GFAP$^+$ astrocytes in 5XFAD mice. ***C***, Representative images showing PKM2 expression colocalizes completely with TREM2 expression near the plaque in 5XFAD mice at 6–7 months. White arrows indicate cells that are positive for both PKM2 and TREM2. (n = 3, 2 M + 1 F) ***D***, Imaris 3D reconstruction images showing colocalization of TREM2 with PKM2 and Iba1.

led to 20% reduction in basal glycolysis in microglia, based on an ECAR assay (Fig. 3*E,F*). Maximum glycolytic capacity was also decreased by 31%, which led to a 50% reduction in glycolytic reserve. In addition, 1 h incubation of rat microglia with TEPP-46 resulted in a 35% reduction in lactate production (Fig. 3*G*). In OCR assays, TEPP-46 had no effect on basal respiration, but reduced maximal respiratory capacity by 24% and spare respiratory capacity by 29% (Fig. 3*H,I*). As a control, we demonstrate that 1 h treatment with TEPP-46 induced tetramerization of PKM2 (Fig. 3*J*). These results may sound opposite to what one expects from TEPP-46 treatment based on the Warburg effect, but a growing literature suggests that the well-accepted positive links between glycolysis with a pro-inflammatory response, and respiratory activity, with an anti-inflammatory response may not be so strict. For instance, under conditions in which PKM2 expression is induced, such as LPS treated macrophages, TEPP-46 treatment significantly reduced IL-1β production (Palsson-McDermott et al., 2015). Similarly, deleting HK2, the first enzyme in glycolysis, from Cx3cr1$^+$ microglia, resulted in reduction in both glycolytic and respiratory function (Hu et al., 2022). We surmise that our data provide additional support for the emerging notion that perturbations in the glycolytic pathway will have an impact not only on glycolysis but also on oxidative phosphorylation under pathological conditions.

Selective deletion of *Pkm2* in microglia leads to reduction in AD pathology in 5XFAD mice

To determine the role of PKM2 in microglial metabolism and its effect on AD pathology, we deleted *Pkm2* from microglia by crossing 5XFAD mice with Cx3cr1-CreERT2$^{+/-}$:PKM2$^{fl/fl}$ mice. Tamoxifen-mediated deletion of PKM2 from microglia was highly effective without causing a huge compensatory increase in its isoform, PKM1, in the experimental FAD:i-PKM2$^{M\Delta}$ mice compared to the control FAD:i-PKM2^{MC} mice (Fig. 4*A,B*). Selective deletion of PKM2 in microglia but not in astrocytes is also confirmed by immunohistochemistry of 4-month-old mouse brain sections from both genotypes (Fig. 4*C*). In regard to its effect on overall AD pathology, deleting PKM2 in microglia resulted in a reduction in AD pathology in 5XFAD mice: Both soluble and insoluble Aβ42 levels were reduced in FAD:i-PKM2$^{M\Delta}$ mice compared to the control via Western blots and ELISA assays at 4–5 months (Fig. 4*D,E*). This reduction was reflected in a decline in amyloid plaque numbers and in their

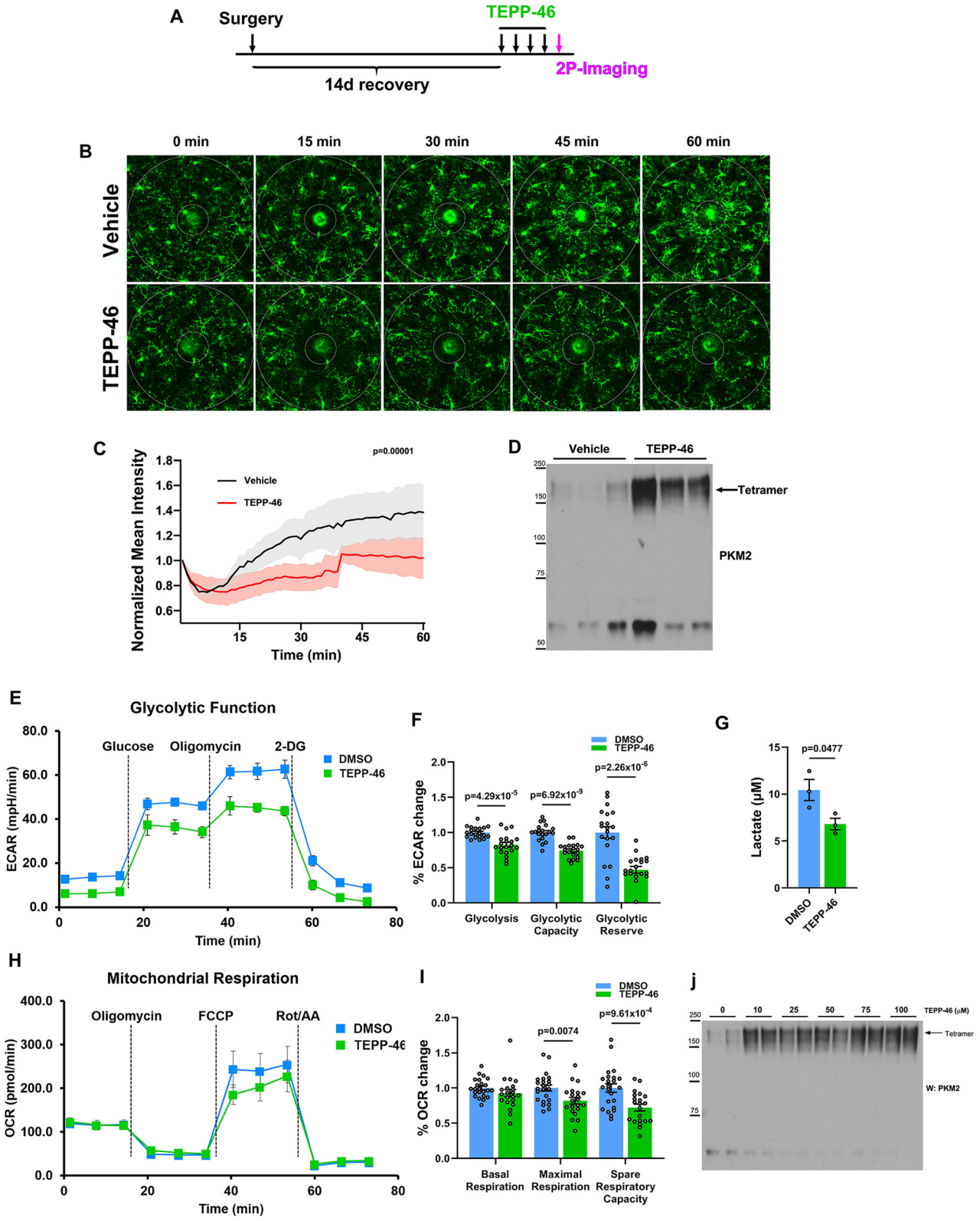

Figure 3. Pharmacological PKM2 activation impaired microglial recruitment as well as glycolysis and oxidative phosphorylation. ***A***, A diagram of experimental time line for two-photon imaging study in ***B–D***. ***B***, Representative images of in vivo two-photon imaging of Cx3cr1-GFP^{+} microglia after laser-induced injury with and without TEPP-46 at 50 mg/Kg daily for 4 d. Smaller circles depict the laser-injury epicenter, while larger images represent the region of interest (ROI), from which quantification of microglial recruitment was calculated for 1 h. ***C***, Quantification of GFP signals in the ROI in (***B***) ($n = 4$, all M, for each treatment group). ***D***, Lysates from isolated microglia from the vehicle or TEPP-46 treated mice were subjected to DSS crosslinking and followed by PKM2 Western blotting ($n = 3$, 2 M + 1 F, for vehicle and $n = 3$, 2 M + 1 F, for TEPP-46 group). ***E***, The effect of TEPP-46 on extracellular acidification rate (ECAR) in primary rat microglial cultures. Rat primary microglia were incubated for 4 h with of 75 μM TEPP-46 prior to ECAR and OCR measurements. ***F***, Quantification of the changes in glycolysis, glycolytic capacity, and glycolytic reserve by TEPP-46 in (***E***) ($n = 3$–5 replicates for each treatment with $n = 4$ independent experiments). ***G***, Changes in lactate concentration in

sizes upon deleting *Pkm2*; the proportion of plaques that were less than 25 μm^2 was significantly higher in FAD:i-PKM2$^{M\Delta}$ mice compared to its control, while the proportion of plaques greater than 250 μm^2 was significantly reduced in FAD:i-PKM2$^{M\Delta}$ mice than in the control (Fig. 4*F,G,H*). In line with these data, the number of active synapses was increased in the stratum oriens of the CA1 region of the hippocampus (Fig. 4*I,J*). Active synapses were defined by synaptic puncta which showed apposing or overlapping PSD95 and vGlut1 signals. These results together suggest that aberrant activation of PKM2 in microglia contributes significantly to AD pathology. This phenotype of FAD:i-PKM2$^{M\Delta}$ mice is almost identical to what was published in Pan et al. (Pan et al., 2022).

Selective deletion of *Pkm2* from microglia in 5XFAD mice leads to activation of DAM phenotype in microglia

Under neurodegenerative conditions, microglia undergo transcriptomic changes that are characterized as homeostatic, DAM1, and DAM2 stages (Keren-Shaul et al., 2017). While TREM2 activation is crucial for developing the DAM2 signature, the signal that induces the change from homeostasis to the DAM1 stage is not clear. Since retaining TREM2, a gene belonging to the DAM2 stage, is protective against AD pathology (Keren-Shaul et al., 2017; Zhou et al., 2020), an increase in DAM gene expression would be regarded as being beneficial in general, bestowing microglia with the correct cellular tools to remove toxic amyloid. We hypothesized that metabolic stress is a signal that regulates the development of the DAM1 signature in microglia. To address whether PKM2 deletion altered DAM signatures in microglia, and whether the analyses would unveil subclusters of microglia that are critical for glucose metabolism, we performed snRNAseq analyses of microglia isolated with Cd11b antibody-conjugated beads from FAD:i-PKM2$^{M\Delta}$ and control FAD:i-PKM2^{MC} mice at 4 months of age using the 10× Genomics Chromium Next GEM Single Cell 3′ Reagent kits (Extended Data Table 5-1). From three mice per genotype, a total of 15,636 and 18,512 cells from FAD:i-PKM2^{MC} and FAD:i-PKM2$^{M\Delta}$ microglia, respectively, were selected for subsequent analyses after QC/filtering steps. Following unbiased cell clustering, 13 distinct cell clusters were identified, which is also shown as UMAP (Fig. 5*A*). Of the 13 clusters, six (namely clusters 0, 1, 2, 3, 4, and 6) were microglial clusters comprising 83.5% and 87.0% of the total from the control and FAD:i-PKM2$^{M\Delta}$ mice, respectively (Fig. 5*B*). A macrophage cluster was also identified as cluster 5, which comprised 9.16% and 7.64% of the total from the control and FAD:i-PKM2$^{M\Delta}$ mice, respectively, reflecting the microglia/macrophage-specific Cx3cr1-CreERT2 line used for the study. The rest of the clusters comprised less than 2% of the total, so they were not included in subsequent analyses. All 6 microglia plus macrophage clusters expressed the *Pkm* gene, and its expression was lowest in cluster 0, while its expression was significantly higher in clusters 4 and 6 (Fig. 5*C* and Extended Data Table 5-2). It should be clarified that upon Cre-mediated recombination, only *Pkm2*-specific exon 10 becomes deleted while leaving the rest of the *Pkm* gene intact, allowing detection of the *Pkm* gene by snRNAseq (Israelsen et al., 2013). When the 484 differentially expressed genes (DEG) were analyzed in a Volcano plot (Extended Data Table 5-3), we found many DAM genes, such as *ApoE*, were among those whose levels increased most upon *Pkm2* deletion, which is highlighted with pink arrows in the Volcano plot (Fig. 5*D*). Individual UMAP feature plots of *ApoE* expression additionally illustrate that *Pkm2* deletion resulted in a substantial increase in *ApoE* expression in clusters 4 and 6 in particular, although its expression was increased in all microglial clusters (Fig. 5*E*). *Trem2* expression was also increased in cluster 4 in FAD:i-PKM2$^{M\Delta}$ mice, although the extent of its increase is much less than that of *ApoE*, probably due to the age at the time of the microglia isolation for snRNAseq, 4 months. *ApoE* expression was shown to precede the expression of *Trem2* in 5XFAD mice (Keren-Shaul et al., 2017). In accordance with the snRNAseq data, we observed ∼2-fold increase in APOE but not TREM2 protein expression in Cd11b^{+} microglia isolated from 4–5 month-old FAD:i-PKM2$^{M\Delta}$ mice (Fig. 5*F,G*).

Changes in all the DAM genes in each of the microglia and macrophage clusters were examined as heatmap analyses. A heatmap plot of DAM genes revealed that ∼75% of them were expressed highly in clusters 4 and 6, with cluster 6 expressing ∼50% of DAM genes (Fig. 6*A*). With *Pkm2* deletion, 38% of homeostatic genes were downregulated in the cluster 6, while 63% of homeostatic genes in the cluster 6 were upregulated. Among DAM stage 1 and 2 genes in clusters 2, 4, and 6%, 81% showed increases, while only 17% showed a decrease upon *Pkm2* deletion (Fig. 6*B*). The majority of genes whose expression increased with *Pkm2* deletion belongs to clusters 4 and 6, which express a higher level of *Pkm* mRNA compared to other microglial clusters, suggesting glucose imbalance, perhaps mediated by the increase in the *Pkm* gene in 5XFAD mice, influences DAM gene expression. A similar pattern of gene expression was observed when we analyzed AD risk genes (Jansen et al., 2019; Kunkle et al., 2019; Schwartzentruber et al., 2021; Wightman et al., 2021; Bellenguez et al., 2022): ∼65% of AD risk genes were highly expressed in cluster 6 (Fig. 6*C*), and *Pkm2* deletion resulted in both up and downregulation of genes (Fig. 6*D*). This is in agreement with a recent report that demonstrated that the sugar metabolism module is also enriched with proteins that are implicated as AD genetic risk factors (Johnson et al., 2020).

We also wanted to compare changes in homeostatic and DAM genes among clusters 2, 4, and 6 from each other in FAD:i-PKM2^{MC} and FAD:i-PKM2$^{M\Delta}$ mice. Changes included both increased and decreased genes upon *Pkm2* deletion. The proportion of expressed homeostatic, DAM1, and DAM2 genes out of the 56 total is presented for clusters of 2, 4, and 6 as pie diagrams (Fig. 6*E*). Between the two genotypes, the proportions in each cluster did not change greatly in each class of homeostatic, DAM1, and DAM2 genes. When we distinguished those that increased, decreased, and were unchanged upon *Pkm2* deletion, however, the differences became obvious (Fig. 6*F*). In cluster 2, a majority of genes did not change, except for some increase in DAM2 genes. In cluster 4, homeostatic genes remained unchanged, while both DAM1 and DAM2 genes increased

←

the media from rat microglial cultures treated for 1 h with vehicle and TEPP-46 ($n = 3$ replicates for each treatment). ***H***, The effect of TEPP-46 on oxygen consumption rate (OCR) in primary rat microglial cultures. ***I***, Quantification of the changes in basal and maximal respiration, and spare respiratory capacity by TEPP-46 in (***H***) ($n = 3$–5 replicates for each treatment with $n = 5$ independent experiments). Data are expressed as mean ± SEM. Paired Student's *t* test was used in (***C***), and unpaired Student's *t* test was used in (***F, G, I***). ***J***, TEPP-46 induced PKM2 tetramers in rat microglia at concentrations ranging from 10 to 100 μM.

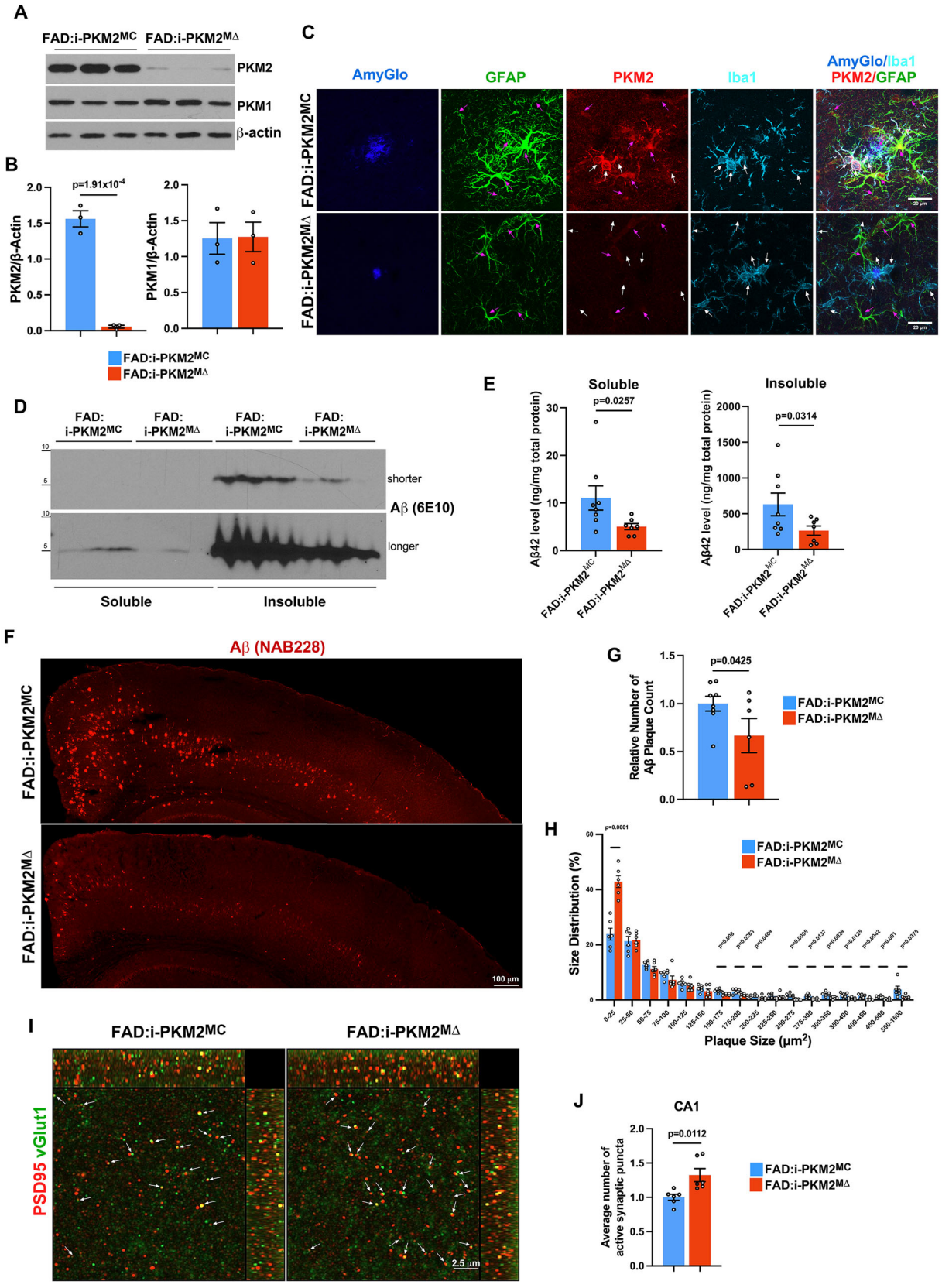

Figure 4. Selective deletion of *Pkm2* in microglia led to reduction in Alzheimer's pathology in 5XFAD mice. ***A***, Western blotting of lysates from microglia isolated from FAD:i-PKM2^{MC} and FAD:i-PKM2^{MΔ} mice at 4–5 months of age. ***B***, Quantification of PKM1 and PKM2 levels in (***A***) ($n = 3$, 2 M + 1 F, for FAD:i-PKM2^{MC} and $n = 3$, 1 M + 2 F, for FAD:i-PKM2^{MΔ} mice). ***C***, Representative images showing PKM2 expression lost selectively in microglia (white arrows) and not in astrocytes (pink arrows). ($n = 3$, 3 M, for FAD:i-PKM2^{MC} and $n = 3$, 2 M + 1 F, for FAD:i-PKM2^{MΔ} mice). ***D***, Western blotting of both soluble and insoluble amyloid β peptides from FAD:i-PKM2^{MC} and FAD:i-PKM2^{MΔ} mice at 4–5 months of age. ***E***, ELISA analysis of both soluble and insoluble Aβ42 levels from FAD:i-PKM2^{MC} and FAD:i-PKM2^{MΔ} mice at 4–5 months of age ($n = 8$, 4 M + 4 F, for FAD:i-PKM2^{MC} and $n = 7$, 2 M + 5 F, for FAD:i-PKM2^{MΔ} mice). ***F***, Representative images of plaques stained for Aβ peptides in the cortex of FAD:i-PKM2^{MC} and FAD:i-PKM2^{MΔ} mice at 4–5 months of age. ***G***, Quantification of the relative number of plaques in FAD:i-PKM2^{MC} and FAD:i-PKM2^{MΔ}

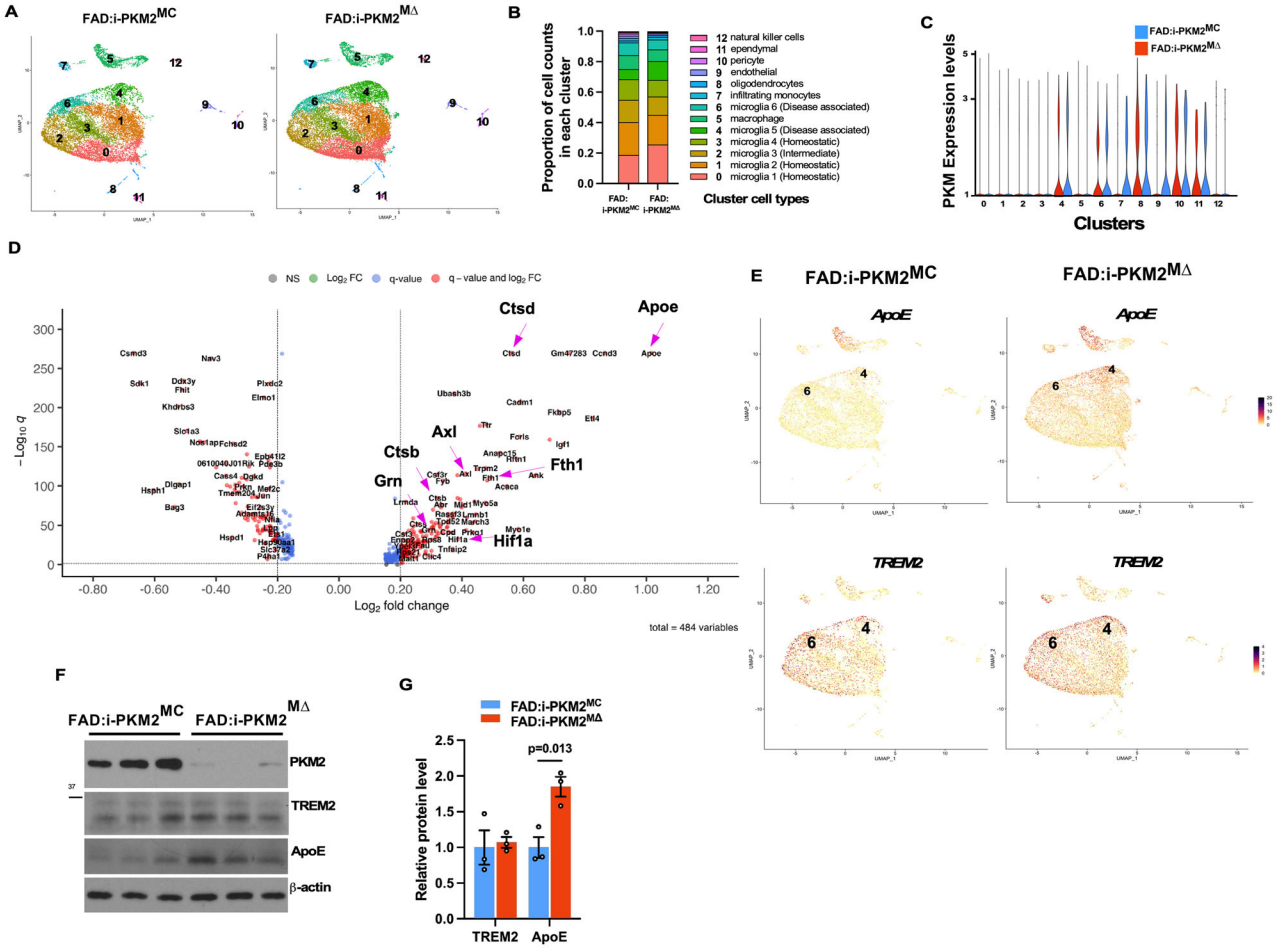

Figure 5. Selective deletion of *Pkm2* in microglia of 5XFAD mice leads to increase in DAM genes. ***A***, Uniform Manifold Approximation and Projection (UMAP) of snRNAseq data from CD11b^{+} microglia purified from 4-month-old FAD:i-PKM2^{MC} and FAD:i-PKM2^{MΔ} mice ($n = 3$, 2 M + 1 F, for each genotype). Microglia are represented in 6 clusters, designated 0, 1, 2, 3, 4, and 6. Based on gene expression profiles, clusters of 0, 1, and 3 represent homeostatic microglia, while clusters 4 and 6 represent disease-associated microglia. Cluster 2 comprises intermediate microglia. Extended Data Table 5-1. Metadata of genes identified by snRNAseq with cluster designation. ***B***, Proportion of cells identified in each cluster. ***C***, Violin plot showing *Pkm* gene expression in each cluster. Extended Data Table 5-2. List of DEG between two genotypes with fold changes. ***D***, Volcano plots of selected genes whose $\log_2$ fold change is either greater than +0.20 or less than −0.20 among microglial clusters ($n = 484$ genes). Genes on the right of the volcano plot represent genes whose expression is increased in FAD:i-PKM2^{MΔ} mice compared to FAD:i-PKM2^{MC} mice. DAM genes are indicated with pink arrows. Extended Data Table 5-3. List of genes utilized for a Volcano plot. ***E***, UMAP analysis of *ApoE* and *TREM2* genes in FAD:i-PKM2^{MC} and FAD:i-PKM2^{MΔ} mice. Clusters of 4 and 6 are indicated. ***F***, Western blots of APOE and TREM2 proteins from CD11b^{+} microglia isolated from 4-month-old FAD:i-PKM2^{MC} and FAD:i-PKM2^{MΔ} mice. ***G***, Quantification of the blots in (***F***) ($n = 3$, 2 M + 1 F for FAD:i-PKM2^{MC} and $n = 3$, 1 M + 2 F for FAD:i-PKM2^{MΔ} mice). Data are expressed as mean ± SEM. Unpaired Student's *t* tests were used in (***G***).

dramatically. Also in cluster 6, large changes were observed, especially with homeostatic genes, all of which showed either an increase or decrease. Like cluster 4, DAM1 genes in cluster 6 increased greatly. A majority of DAM2 genes on the other hand remained unchanged, although some showed an increase. These results highlight our notion that *Pkm2* deletion resulted in a significant increase in DAM1 genes, especially in clusters 4 and 6. Quantitative PCR analyses of selective AD risk and DAM genes using RNA from isolated microglia confirmed the snRNAseq data (Fig. 6*G*). Based on these data, we surmised clusters 4 and 6 are good candidates for metabolic microglia clusters.

Cluster 6 is metabolic microglia cluster

IPA using 15 top canonical cellular pathways revealed that cluster 6 differs from the other microglial clusters: When comparing the plots for cluster 6 to clusters 0 to 5, for each criterion of biological function, cluster 6 exhibits a generally reversed relationship for each *z*-score sign and magnitude. In more detail, the genes whose levels increased in clusters 0 to 5 include those that play roles in RhoGDI signaling, PPAR signaling, PTEN signaling, VDR/RXR activation, PPARα/RXRα activation, and cell cycle regulation. The genes whose levels increased in cluster 6 on the other hand included those for adherens junction, CDC42 signaling, spliceosomal cycle, AMPK

←

mice at 4–5 months of age ($n = 8$, 5 M + 3F, for FAD:i-PKM2^{MC} and $n = 6$, 2 M + 4F, for FAD:i-PKM2^{MΔ} mice). ***H***, Average size distribution of plaques in FAD:i-PKM2^{MC} and FAD:i-PKM2^{MΔ} mice at 4–5 months of age ($n = 6$, 5 M + 1 F, for FAD:i-PKM2^{MC} and $n = 6$, 2 M + 4 F, for FAD:i-PKM2^{MΔ} mice). ***I***, Representative images of active synaptic puncta that were stained with vGlut1 and PSD95 in the hippocampus of FAD:i-PKM2^{MC} and FAD:i-PKM2^{MΔ} mice at 4–5 months of age. Arrows indicate active synaptic puncta with overlapping or closely juxtaposed vGlut1 and PSD95 immunoreactivity. ***J***, Quantification of active synaptic puncta from FAD:i-PKM2^{MC} and FAD:i-PKM2^{MΔ} mice at 4–5 months of age ($n = 6$, 5 M + 1 F, for FAD:i-PKM2^{MC} and $n = 6$, 2 M + 4 F, for FAD:i-PKM2^{MΔ} mice). Data are expressed as mean ± SEM. Unpaired Student's *t* tests were used in (***B, E, G, H, J***).

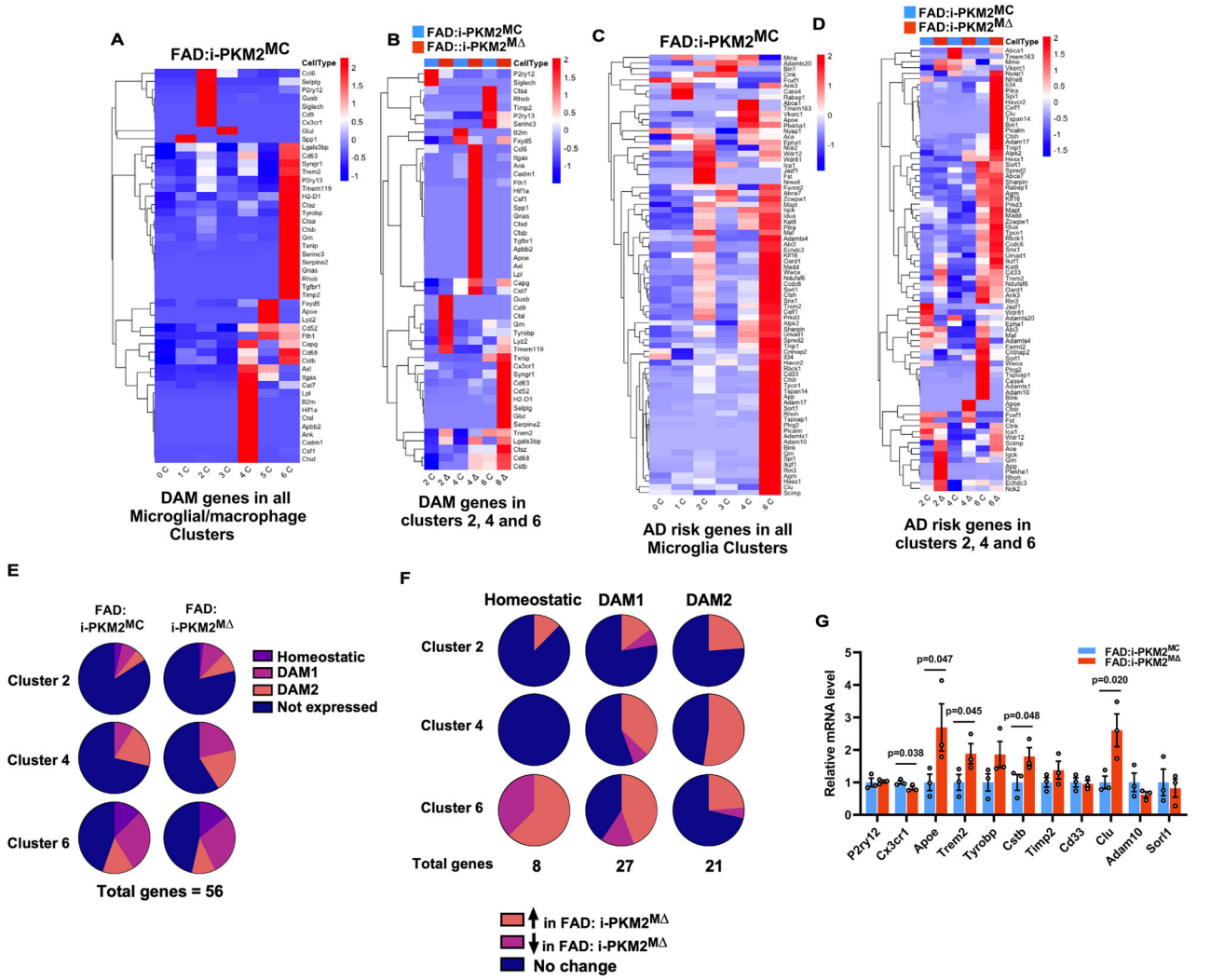

Figure 6. Selective microglia deletion of *Pkm2* in 5XFAD mice leads to activation of DAM phenotype in microglia. ***A***, Heatmap analysis of DAM genes in all microglial clusters plus the macrophage cluster 5 in FAD:i-PKM2^{MC} mice. ***B***, Heatmap analysis of DAM genes in clusters 2, 4, and 6 in both genotypes. ***C***, Heatmap analysis of AD risk genes in all microglial clusters in FAD:i-PKM2^{MC} mice. ***D***, Heatmap analysis of AD risk genes in clusters 2, 4, and 6 in both genotypes. ***E***, Pie diagrams of the proportion of homeostatic and DAM genes expressed in microglial clusters of 2, 4, and 6 from both genotypes. ***F***, Pie diagrams showing the proportion of homeostatic and DAM genes whose expression levels were changed upon *Pkm2* deletion in clusters of 2, 4, and 6. ***G***, qPCR analyses of selected DAM and AD risk genes which were identified to show changes in mRNA levels ($n = 3$, 2 M + 1 F for each genotype). Data are expressed as mean ± SEM. Unpaired Student's *t* test was used in (***G***).

signaling, autophagy, RAC signaling, PLC signaling, and the senescence pathway (Fig. 7*A*). *Pkm2* deletion did not alter these distinct features of cluster 6 greatly, except for the strength of each pathway. As a way to validate the significance of the IPAs, we analyzed whether the extent of AMPK activation, a major metabolic regulator of global cellular energy homeostasis, was altered in microglia by performing Western blotting of proteins extracted from Cd11b^{+} microglia from FAD:i-PKM2^{MC} and FAD:i-PKM2^{MΔ} mice. *p*-AMPKα and *p*-ACC levels were elevated significantly in FAD:i-PKM2^{MΔ} compared to those in FAD:i-PKM2^{MC} mice (Fig. 7*B, C*), suggesting *Pkm2* deletion had an effect on AMPK activation. Although this data does not derive exclusively from cluster 6 microglia *per se*, it should be regarded as included. We thus conclude that cluster 6 microglia are unique in their signaling capacity, including the AMPK pathway. This data corresponds well with the report that PKM knockdown increased AMPKα phosphorylation in cancer cell lines (Prakasam et al., 2017).

Cluster 6 also stood out when we performed CellChat analysis with DEG from microglial/macrophage clusters (Jin et al., 2021): CellChat analysis identified 12 shared ligand-receptor interactions with high significance (Fig. 8*A*). From the CellChat analyses, we focused on Axl signaling via ProS/Gas6, since not only *Axl* expression increased dramatically in cluster 6 in FAD:i-PKM2^{MΔ} compared to that in FAD:i-PKM2^{MC} mice (Fig. 8*B,C*), but also its signaling capacity increased dramatically in cluster 6 in FAD:i-PKM2^{MΔ} compared to that in FAD:i-PKM2^{MC} mice (Fig. 8*D*). Axl is a member of the Tyro3-Axl-Mer (TAM) receptor family, involved in engulfing amyloid plaques (Huang et al., 2021). We hypothesized that Axl expression and signaling may represent a cluster 6-mediated event. Indeed, Axl expression colocalized with PKM2 among microglia that were near a plaque, and not with microglia that were not associated with plaques (Fig. 8*E*). In addition, we observed an increase in *p*-Axl/Axl signals from the extracts isolated from microglia from FAD:i-PKM2^{MΔ} compared to FAD:i-PKM2^{MC} mice (Fig. 8*F,G*). Although we could not tell if Axl activation occurs in cluster 6 at this time, these results together support the notion that cluster 6 differs from other microglial/macrophage clusters. We thus interpret these data as suggesting that microglia

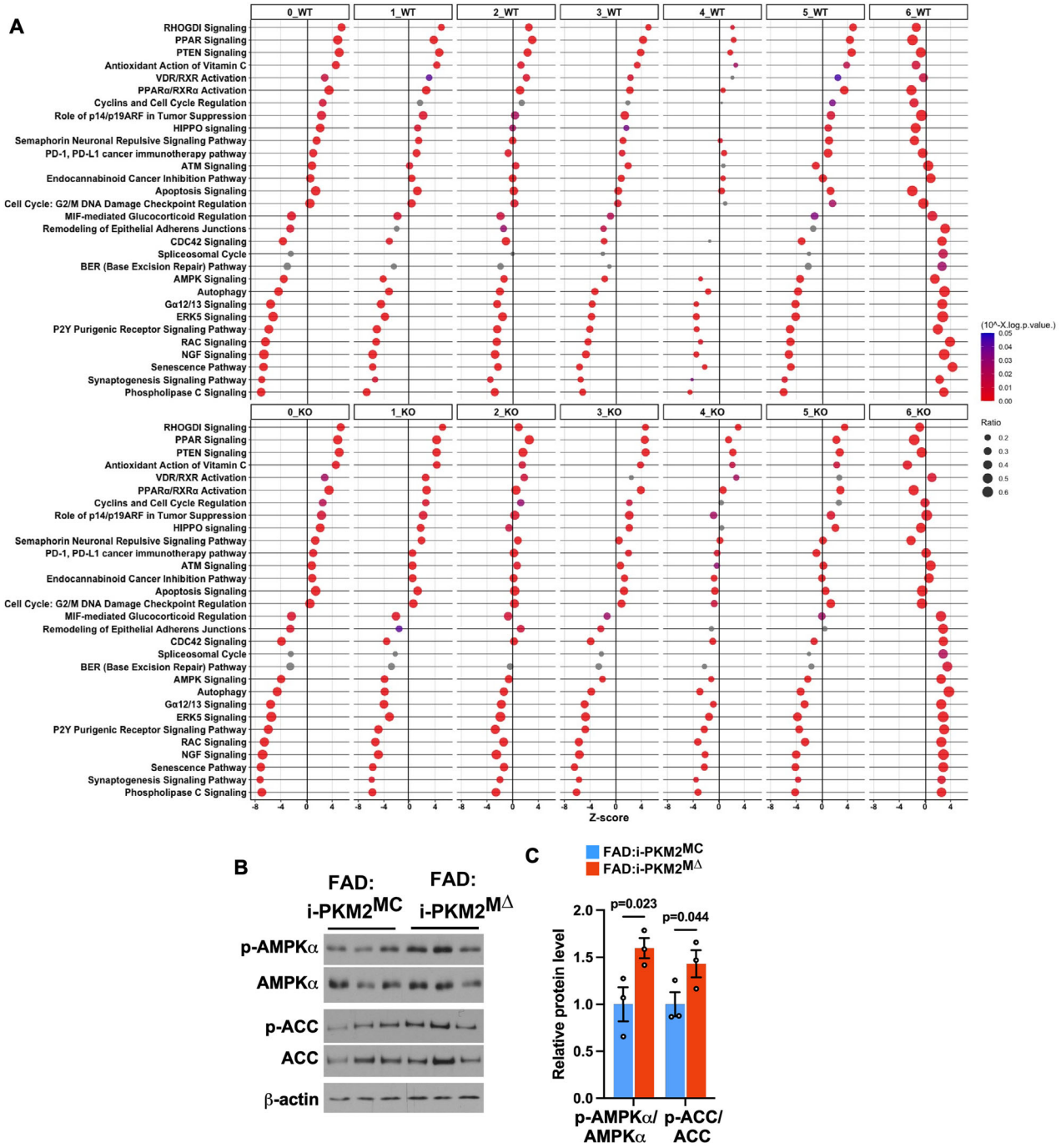

Figure 7. The cluster 6 is distinct from other clusters. ***A***, IPA of the top 15 canonical pathways of clusters 0 to 6 in FAD:i-PKM2^{MC} and FAD:i-PKM2$^{M\Delta}$ mice. ***B***, Western blots of *p*-AMPKα, AMPKα, *p*-ACC, and ACC from CD11b^{+} microglia isolated from 4-month-old FAD:i-PKM2^{MC} and FAD:i-PKM2$^{M\Delta}$ mice. ***C***, Quantification of the blots in (B) ($n = 3$, 1 M + 2 F for FAD:i-PKM2^{MC} and $n = 3$, 2 M + 1 F for FAD:i-PKM2$^{M\Delta}$ mice). Data are expressed as mean ± SEM. Unpaired Student's *t* test was used in (***C***).

belonging to cluster 6 are among those that are actively recruited to amyloid plaques, where they phagocytose amyloid β and efferocytose damaged cells. In accordance with the data, ~64% of phagocytic genes were expressed in cluster 6 (Fig. 8*H*).

Cluster 6 contains genes involved in glycolysis and TCA cycle

In support of our hypothesis that cluster 6 is a metabolic cluster, we found that a majority of genes in the glycolytic pathway and in TCA cycles are enriched in cluster 6 (Fig. 9*A,C*). Upon deleting *Pkm2*, expression of more than 50% of the genes increased further in cluster 6 (Fig. 9*B,D*), suggesting a crucial role of PKM2 in metabolic environment in cluster 6 microglia. When we analyzed glycolytic enzyme expression in Cd11b^{+} microglial extracts from FAD:i-PKM2^{MC} and FAD:i-PKM2$^{M\Delta}$ mice, the increase upon *Pkm2* deletion was reflected only among HK1, LDHa, and PDH, but not in HK2 and GAPDH, although their mRNA expression levels from snRNAseq data were increased in FAD:i-PKM2$^{M\Delta}$ mice (Fig. 9*E,F*). Among enzymes from the TCA cycle, malate dehydrogenase 2 (MDH2) protein levels were increased in FAD:i-PKM2$^{M\Delta}$ mice compared to its control, while citrate synthase (CS) protein levels did not show a statistically significant difference (Fig. 9*G,H*). We interpret these results as

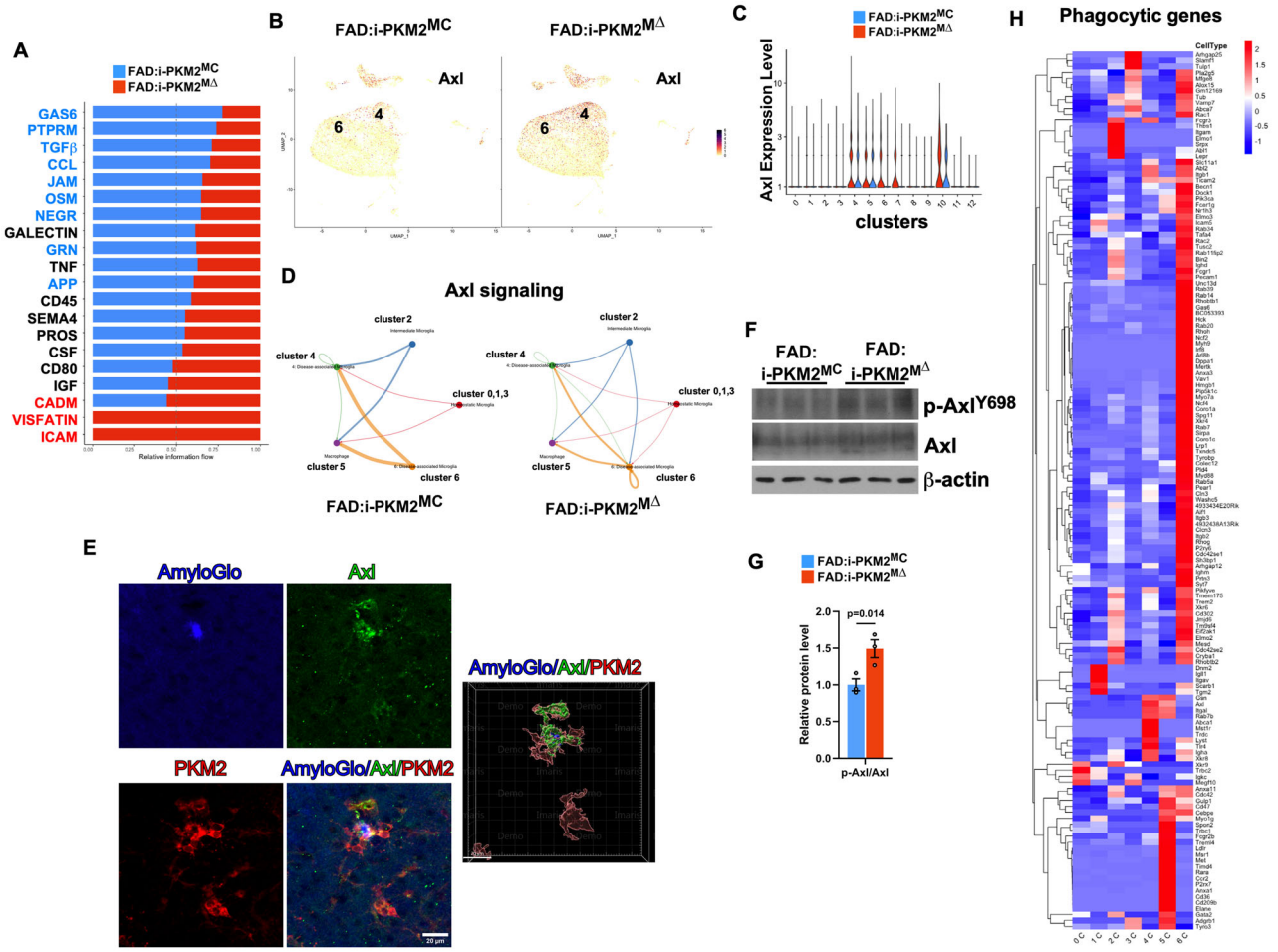

Figure 8. The cluster 6 is enriched with phagocytic genes. ***A***, Identification of ligand-receptor pairs whose interactions were significantly different between the genotypes. Note that genes in black were not significant, while those in blue and red were significantly enriched in FAD:i-PKM2^{MC} and FAD:i-PKM2$^{M\Delta}$ mice, respectively. ***B***, UMAP analysis of *Axl* gene in FAD:i-PKM2^{MC} and FAD:i-PKM2$^{M\Delta}$ mice. Clusters of 4 and 6 are indicated. ***C***, Violin plot showing *Axl* gene expression in each cluster. ***D***, Comparison of Axl signaling between FAD:i-PKM2^{MC} and FAD:i-PKM2$^{M\Delta}$ mice. Edge colors are consistent with the sources of sender and the thicker edge lines indicate stronger signals. ***E***, Representative images showing the colocalization of Axl and PKM2 in plaque-associated microglia in 5XFAD mice (left). Imaris 3D reconstruction image is also shown (right). ***F***, Western blots of *p*-Axl and Axl from CD11b^{+} microglia isolated from FAD:i-PKM2^{MC} and FAD:i-PKM2$^{M\Delta}$ mice. ***G***, Quantification of the *p*-Axl/Axl levels in (***F***) ($n = 3$, 1 M + 2 F for FAD:i-PKM2^{MC} and $n = 3$, 2 M + 1 F for FAD:i-PKM2$^{M\Delta}$ mice). Data are expressed as mean ± SEM. Unpaired Student's *t* test was used. ***H***, Expression levels of genes involved in phagocytosis in microglial/macrophage clusters in FAD:i-PKM2^{MC} mice.

suggesting that PKM2 deletion influences not only glycolytic but also TCA cycle enzyme levels in microglia.

Pkm2 deletion leads to restoration of both glycolytic and respiratory capacity in adult microglia from 5XFAD mice

We decided to perform functional assays to measure changes in glycolysis and mitochondrial respiration with *Pkm2* deletion by employing a Seahorse analyzer. For this, we immuno-purified Cd11b^{+} microglia at 6 weeks from both genotypes and measured both ECAR and OCR. Microglia from FAD:i-PKM2$^{M\Delta}$ mice exhibited a significant increase in both basal and maximal glycolytic capacity in ECAR assays; basal glycolysis increased by 79% and maximal glycolytic capacity by 2-fold (Fig. 10*A*,*B*). Glycolytic reserve was increased but not significantly. These results are opposite to rat primary microglia treated with a PKM2 metabolic activator, TEPP-46, where basal glycolysis, glycolytic capacity, and glycolytic reserve were reduced (Fig. 3*E*,*F*,*G*). These results suggest that metabolic activation of PKM2 is inhibiting overall microglial glycolytic capacity without affecting glycolytic reserve. Regarding mitochondrial respiration, *Pkm2* deletion did not have any effect on basal respiration, but increased maximal respiration by 31%, which resulted in a 50% increase in spare respiratory capacity (Fig. 10*C*,*D*). These results are again opposite to those from rat microglia treated with TEPP-46, where basal respiration was unaffected, while the maximal respiration and respiratory reserve were reduced (Fig. 3*H*,*I*). These results suggest that metabolic activation of PKM2 has a negative effect on respiration as well as on glycolysis. In particular, the 50% increase in respiratory reserve but not glycolytic reserve observed with *Pkm2* deletion is surprising, since it suggests that when there is an emergency metabolic demand for ATP, microglia are likely to utilize mitochondrial respiration rather than glycolysis (Marchetti et al., 2020). We caution, however, that we cannot rule out the possibility that the bioenergetics differ based on the species difference, namely between primary rat and mouse cultures.

We next asked whether microglial mitochondria exhibited any structural changes in 5XFAD mice and whether *Pkm2* deletion had any effect on them. To address this question, we performed transmission electron microscopy (TEM) analyses of freshly immuno-purified and immediately fixed Cd11b^{+} bead-isolated microglia from both genotypes. We found that the length, width and total area of mitochondria were not very different between the two genotypes, but cristae appeared bulged

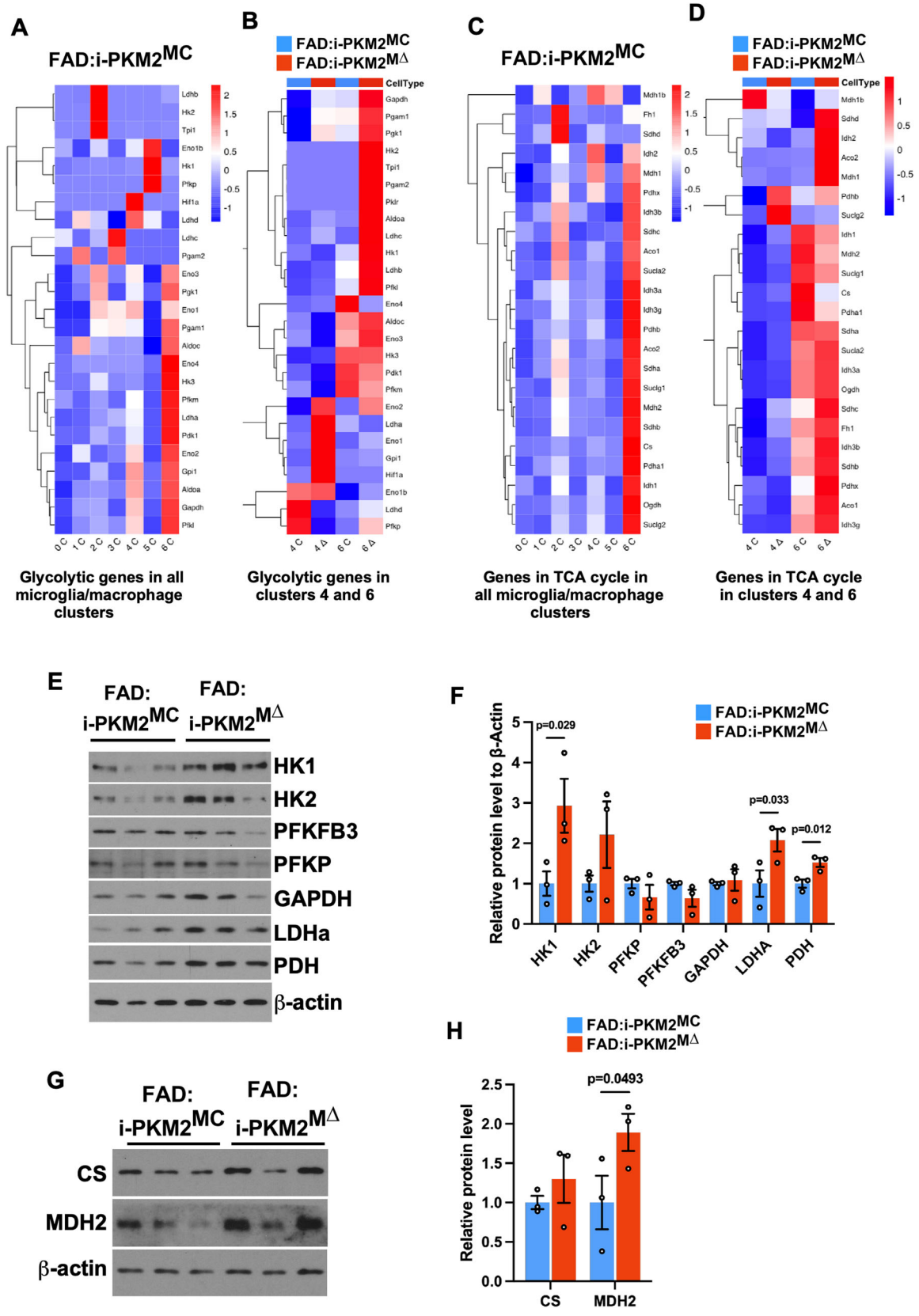

Figure 9. *Pkm2* deletion in microglia resulted in increase in glycolytic and respiratory genes. ***A***, Heatmap analyses of genes for glycolysis in all microglial clusters plus the macrophage cluster 5 in FAD:i-PKM2^{MC} mice. ***B***, Heatmap analyses of genes for glycolysis in clusters 4 and 6 in both genotypes. ***C***, Heatmap analyses of genes for TCA cycle in all microglial clusters plus the macrophage cluster 5 in FAD:i-PKM2^{MC} mice. ***D***, Heatmap analyses of genes for TCA cycle in clusters 4 and 6 in both genotypes. ***E***, Western blots of selected glycolytic enzymes from CD11b^{+} microglia isolated from 4-month-old FAD:i-PKM2^{MC} and FAD:i-PKM2^{MΔ} mice. HK1, hexokinase 1; HK2, hexokinase 2; PFKFB3, 6-phosphofructo-2-kinase/fructose-2,6-biphosphatase 3; PFKP, phosphofructokinase, platelet; GAPDH, glyceraldehyde-3-phosphate dehydrogenase; LDHa, lactate dehydrogenase a; PDH, pyruvate dehydrogenase. ***F***, Quantification of the blots

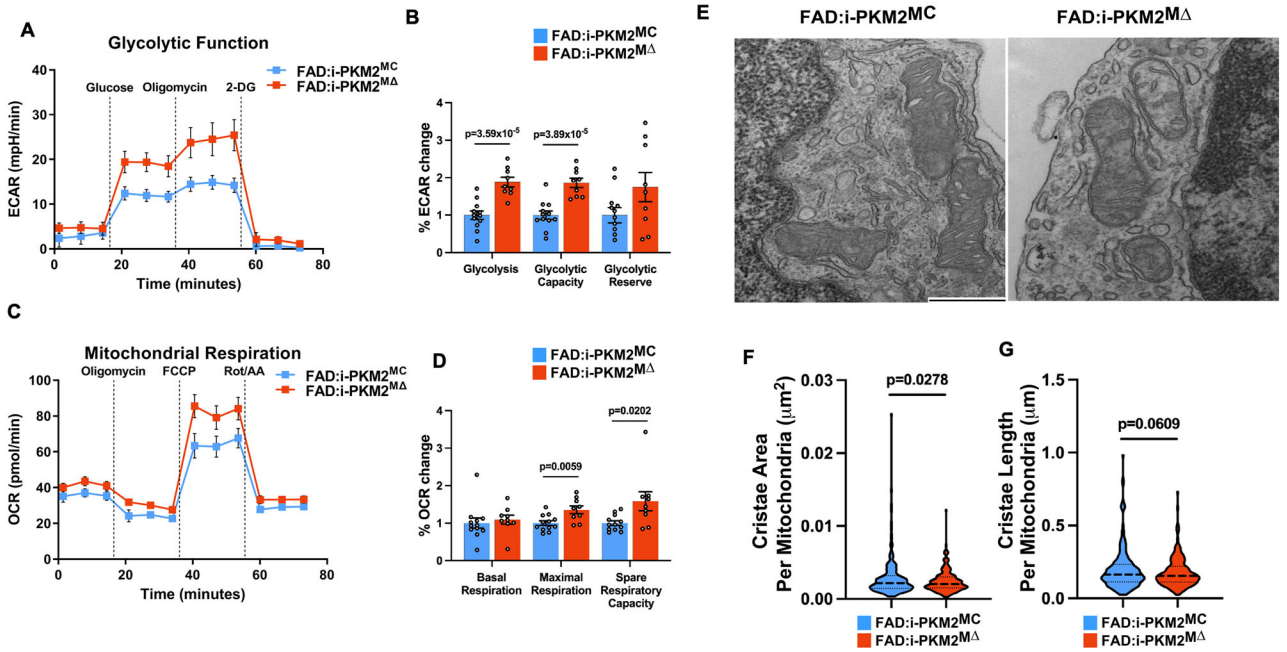

Figure 10. *Pkm2* deletion in microglia resulted in increase in glycolytic and respiratory capacity. ***A***, A representative graph showing the measurement of ECAR in cultured CD11b$^+$ microglia isolated from 6-week-old FAD:i-PKM2^{MC} and FAD:i-PKM2$^{M\Delta}$ mice. ***B***, Quantification of the changes in glycolysis, glycolytic capacity, and glycolytic reserve by *Pkm2* deletion from (***A***) ($n = 5$ replicates for each genotype in $n = 2$ independent experiments). ***C***, A representative graph showing the measurement of OCR in cultured CD11b$^+$ microglia isolated from 6-week-old FAD:i-PKM2^{MC} and FAD:i-PKM2$^{M\Delta}$ mice. ***D***, Quantification of the changes in basal and maximal respiration, and spare respiratory capacity by *Pkm2* deletion from (***C***) ($n = 5$ replicates for each genotype in $n = 2$ independent experiments). ***E***, Representative transmission electron microscopy (TEM) images showing the structure of mitochondria in CD11b$^+$ microglia freshly isolated from 4-month-old FAD:i-PKM2^{MC} and FAD:i-PKM2$^{M\Delta}$ mice. ***F***, Violin plot showing quantification of the average cristae area per mitochondria in (***E***). ***G***, Violin plot showing quantification of the average cristae length per mitochondria in (***E***). Data are expressed as mean ± SEM. Unpaired Student's *t* test was used in (***B, D, F, G***).

in FAD:i-PKM2^{MC} mitochondria rather than the normal thin doublets in FAD:i-PKM2$^{M\Delta}$ mitochondria (Fig. 10*E*). Quantification of the cristae revealed the average cristae area in each mitochondrion was significantly reduced as well as their length in FAD:i-PKM2$^{M\Delta}$ mitochondria, although the length reduction was not statistically significant (Fig. 10*F,G*). Since mitochondrial respiration is intimately linked to cristae, these results demonstrate that 5XFAD mice exhibit a defect in mitochondrial respiration in part by metabolic activation of PKM2, as the defect in respiration in the microglia of 5XFAD mice becomes somewhat corrected by deleting *Pkm2*. A mitochondrial respiratory defect has been reported in AD mice (Yao et al., 2009), although these data were from total brain mitochondria and not just microglia.

In situ spatial metabolomics analyses of plaque-bearing microglia in 5XFAD mice suggest increased respiratory activity upon *Pkm2* deletion

We decided to address the contribution of glycolysis and/or mitochondrial respiration on microglial function by directly measuring microglial metabolites in situ, employing matrix-assisted laser desorption/ionization mass spectrometry imaging (MALDI-MSI). Brain metabolism does not differ wildly in living animals, and MALDI is capable of identifying subtle sample by sample differences over thousands of data points from a brain. In addition, the approach obviates the need to isolate microglia during which process small metabolites can be lost. With combined MALDI-MSI and immunohistochemistry, we analyzed the abundance of a majority of glycolytic and TCA cycle metabolites among plaque-bearing or plaque-associated microglia in the cortex, hippocampus, and subiculum of FAD:i-PKM2^{MC} and FAD:i-PKM2$^{M\Delta}$ mice. The pyruvate data are shown as an example in Figure 11*A*, with a high-magnification view used for quantification after overlaying both Iba1 IHC results and Amylo-Glo plaque staining (Fig. 11*B*). We quantified the abundance of pyruvate in Iba1$^+$ microglia that bear or are close to Amylo-Glo$^+$ plaques, and the results demonstrated a significant reduction in FAD:i-PKM2$^{M\Delta}$ mice (Fig. 11*C*), which was as expected, since pyruvate is the direct product of PKM2. Also shown are all the metabolites that were measured in Figure 11*D, E,* and *F*. A summary of glycolytic and TCA cycle metabolites data is shown in Figure 12*A*. While pyruvate and glyceraldehyde-3-phosphate levels were altered in FAD:i-PKM2$^{M\Delta}$ microglia, most glycolytic metabolites did not show great changes. On the other hand, citrate, cis-aconitate, and malate levels were decreased in FAD:i-PKM2$^{M\Delta}$ microglia in addition to derivatives of oxaloacetate, such as aspartate and N-acetylaspartate as well as glutamate and glutamine that are derived from α-ketoglutarate (Fig. 12*A*). These results are in agreement with the 50% increase observed in respiratory but not glycolytic reserve with *Pkm2* deletion in microglia (Fig. 10).

Our hypothesis is that metabolic stress is one of the key signals that inhibit homeostatic microglia from transitioning into the DAM1 stage. Since our results suggest that aberrant PKM2

←

in (***E***) ($n = 3$, 1 M + 2 F for FAD:i-PKM2^{MC} and $n = 3$, 2 M + 1 F for FAD:i-PKM2$^{M\Delta}$ mice). ***G***, Western blots of CS, citrate synthase and MDH2, malate dehydrogenase 2 from CD11b$^+$ microglia isolated from 4-month-old FAD:i-PKM2^{MC} and FAD:i-PKM2$^{M\Delta}$ mice. ***H***, Quantification of the blots in (***G***) ($n = 3$, 1 M + 2 F for FAD:i-PKM2^{MC} and $n = 3$, 2 M + 1 F for FAD:i-PKM2$^{M\Delta}$ mice). Unpaired Student's *t* test was used in (***F, H***).

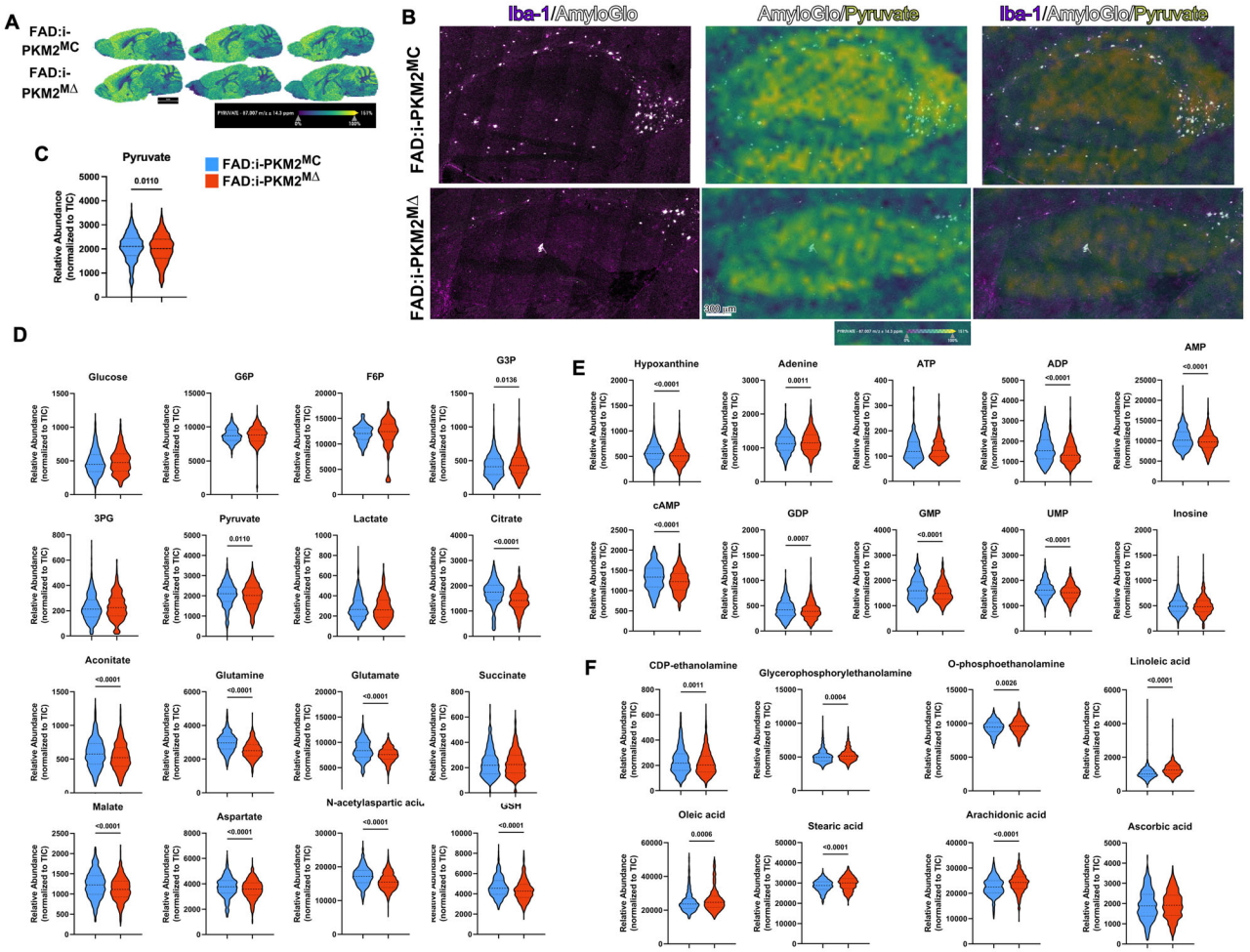

Figure 11. In situ spatial metabolomics assays to measure metabolite abundance among microglia that are associated with plaques. ***A***, Representative matrix-assisted laser desorption/ionization mass spectrometry (MALDI-MSI) images showing the abundance of pyruvate in the sagittal brain sections of FAD:i-PKM2^{MC} and FAD:i-PKM2^{MΔ} mice at 4–5 months of age. ($n = 3$, all F, for each genotype). ***B***, Representative MALDI-MSI images showing the overlay of the abundance of pyruvate among Iba1^{+}, Amylo-Glo^{+} plaque-associated microglia in the hippocampus of FAD:i-PKM2^{MC} and FAD:i-PKM2^{MΔ} mice. ***C***, Violin plot showing quantification of the relative abundance of pyruvate in Iba1^{+}, Amylo-Glo^{+} plaque-associated microglia in selected cortex, hippocampus, and subiculum regions. ***D–F***, Violin plots showing quantification of the relative abundance of metabolites involved in glycolysis and TCA cycle (***D***), in nucleic acid metabolism (***E***), and in lipid metabolism as well as other metabolites (***F***). Data are expressed as mean ± SEM. Unpaired two-tailed Student's *t* tests were used (***C, D, E, F***).

activation disrupts not only glycolytic capacity but also depletes respiratory reserve that can be drawn from when ATP demand is high in microglia (Marchetti et al., 2020), we asked whether inducing glycolytic and/or respiratory metabolic stress would change mRNA levels of *ApoE* and *Trem2* in rat primary microglial cultures. Modulating respiratory capacity alone with IACS-010759, which inhibits the complex I of the electron transport chain, or DCA, which in turn facilitates oxidative phosphorylation at the expense of glycolysis by disinhibiting pyruvate dehydrogenase (Bonnet et al., 2007) did not have any effect (Fig. 12*B,C*). TEPP-46 and 2-DG, both of which have an impact on glycolysis and oxidative phosphorylation, however, reduced both *ApoE* and *Trem2* mRNA levels by 32–36% and 40–52%, respectively. We interpret these results as suggesting that both proper glycolytic and respiratory inputs are necessary to induce DAM1 stage genes in microglia.

Discussion

Although metabolic dyshomeostasis in the brain has been recognized as an important factor in AD pathology, it has not been clear whether this was due to a brain-wide defect in glucose metabolism or a dysfunction in a particular cell type. Here we report that reversing the metabolic defect in one group of cells, microglia, led to a protective effect against AD pathology in 5XFAD mice. Although our results do not rule out contributions from other cell types, whose own metabolic dysfunction could influence overall AD pathology, the reduction in AD pathology observed in 5XFAD mice with microglial *Pkm2* deletion suggests that at a minimum, the metabolic health of microglia themselves is critically important. Along with recent reports that microglia are the major cell types that take up glucose, and the microglial activation state correlates with FDG uptake in human cases (Xiang et al., 2021), our report highlights the importance of maintaining the metabolic heath of microglia in overall AD pathology.

Here, our snRNAseq analyses have identified 6 microglial clusters, clusters 0, 1, 2, 3, 4, and 6. This is twice the number of clusters that were initially identified in 5XFAD mice (Keren-Shaul et al., 2017). The difference is likely due to a larger number of microglia that were sequenced in our study, 15–18,000, compared to 8,000 cells sequenced in Keren-Shaul et al. (2017). In addition, of their 8,000 cells, ~6,000 were microglia, while 13–16,000 were microglia in our study. Perhaps due to an increase in the number of microglial cells sequenced, we have identified the distinct cluster 6 in our study. Not only are about half of all

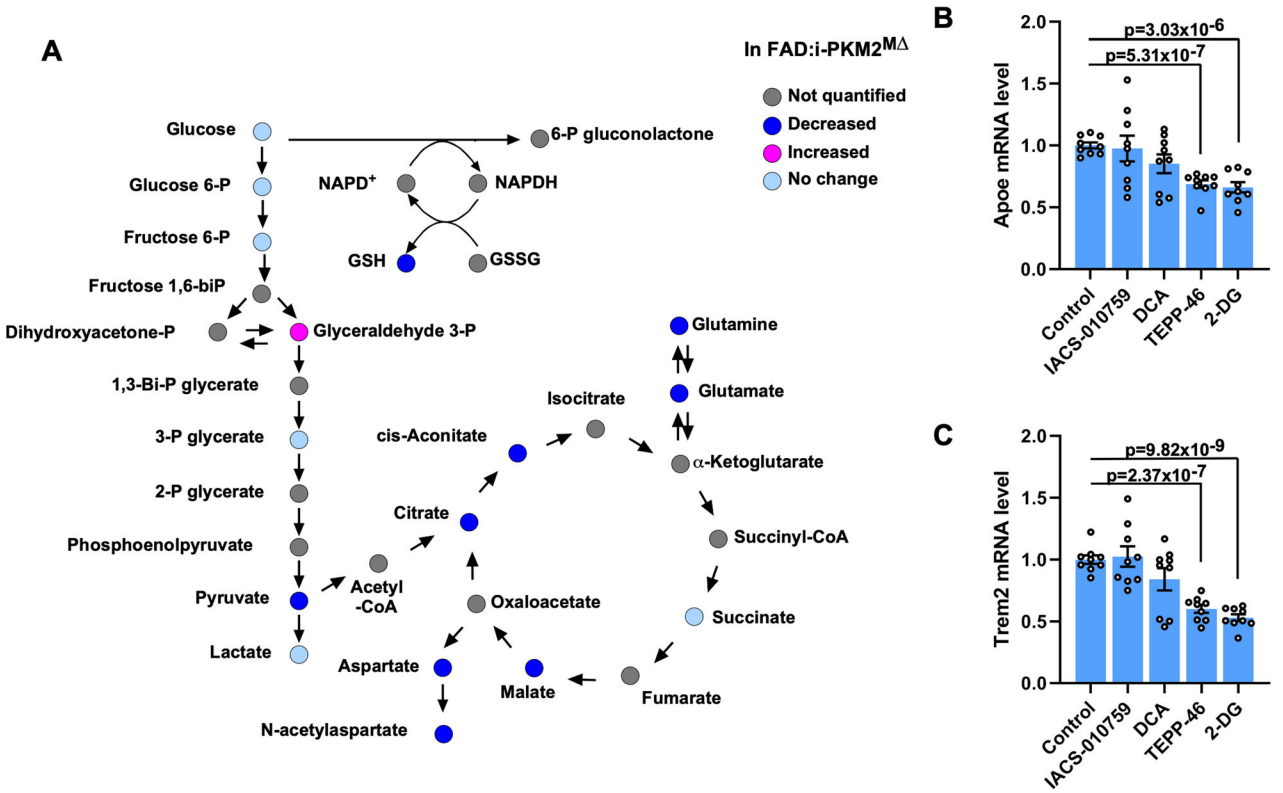

Figure 12. In situ spatial metabolomics analyses revealed an increase in the flux of TCA metabolites in plaque-associated microglia in the absence of *Pkm2*. ***A***, Summary of the changes of glycolytic and TCA metabolites in Iba1^{+}, AmyIo-Glo^{+} plaque-associated microglia quantified by MALDI-MSI in FAD:i-PKM2$^{M\Delta}$ mice compared to FAD:i-PKM2^{MC} mice. ***B***, qPCR analyses showing changes in *ApoE* mRNA levels after metabolic stress in rat primary microglial cultures ($n = 9$ replicates for each treatment from 3 independent experiments). ***C***, qPCR analyses showing changes in *Trem2* mRNA levels after metabolic stress in primary rat microglial cultures ($n = 9$ replicates for each treatment from 3 independent experiments). Data are expressed as mean ± SEM. Unpaired Student's *t* tests were used in (***B, C***).

DAM genes and AD risk genes expressed in cluster 6, but also expression is higher in cluster 6 of genes for glycolysis and TCA cycle, perhaps behaving as a metabolic cluster. Enrichment of metabolic genes in cluster 6 may suggest that it is metabolically more active than other microglial clusters. An increase in AMPK signaling in cluster 6 from IPAs as well as actual detection of increased *p*-AMPKα and *p*-ACC levels in isolated microglia may be regarded as supporting this contention.

We found that microglia in 5XFAD mice have mitochondrial alterations with enlarged cristae structure, and *Pkm2* deletion at least partially corrected it. Mitochondria are known to function as a signaling organelle in addition to being responsible for bioenergetics, releasing metabolites of the TCA cycle (Weinberg et al., 2015). These metabolic intermediates also function as signaling molecules influencing cell phenotypes especially in immune cells, such as succinate, which has been implicated in pro-inflammatory macrophage responses (Mills et al., 2016). A prevailing view was that a glycolytic switch was necessary for the inflammatory state in immune cells, while oxidative phosphorylation and fatty acid oxidation accompanied protective anti-inflammatory differentiation (Vats et al., 2006; Huang et al., 2016; Mills et al., 2016; Tannahill et al., 2013). These studies, however, relied on isolated immune cells rather than investigating the bioenergetics in intact tissues. Even with macrophages in tissue preparations, isolated from individual organs rather than collecting circulating macrophages, bioenergetic analyses unveiled stark differences among macrophages in different organs (Wculek et al., 2023): the authors perturbed oxidative phosphorylation by deleting *Tfam* in an organ-specific manner and discovered that oxidative phosphorylation rather than glycolysis was central in macrophage differentiation. This demonstrates that immune cells are metabolically plastic, adjusting their metabolic responses depending on need in their immediate microenvironment. In our study, we sought to avoid the need to isolate microglia at all by employing in situ spatial metabolomics on intact mouse brain sections. Our data illustrated that *Pkm2* deletion in microglia of 5XFAD mice exhibited reduction in TCA intermediates, e.g., an increased TCA cycle activity (Buescher et al., 2015; Niedenfuhr et al., 2015), while changes in the glycolytic metabolites were relatively minor. In addition, we found that there were significant changes in some of the fatty acids, such as linoleic acid, oleic acid, stearic acid, arachidonic acid as well as ethanolamines (Fig. 11*F*), which we interpret as suggesting increased demand of fatty acid oxidation in FAD:i-PKM2$^{M\Delta}$ microglia as it is typically associated with increased oxidative phosphorylation (Weinberg et al., 2015).

We found that HK2 protein levels increased in 5XFAD mice compared to WT controls and also with *Pkm2* deletion, although the increase was not statistically significant in the latter case. Additionally, its mRNA expression is enriched in cluster 2 in FAD:i-PKM2^{MC} microglia but becomes enriched in cluster 6 in FAD:i-PKM2$^{M\Delta}$ microglia (Fig. 9*A,B*). HK2 is a key enzyme in glycolysis converting glucose to glucose-6-phosphate. It has been shown recently that HK2 is also expressed highly in microglia under neuropathological conditions including AD (Hu et al., 2022). When *Hk2* was deleted with the same Cx3cr1-CreERT2 as we have used here, they observed a decrease in both glycolytic and respiratory capacity. This is similar to our data with *Pkm2*

deletion, which resulted in influencing both glycolysis and respiration (Fig. 10), albeit the fact that the effect of *Hk2* and *Pkm2* deletion on glycolysis and respiration are opposite to one another, possibly due to the fact that PKM2 can function as a metabolic regulator as a tetramer as well as a transcription factor in the monomer/dimer form. Nonetheless, these results suggest that perturbations in the glycolytic pathway will have an impact on not only glycolysis but also on oxidative phosphorylation.

Very recently, Pan et al. (2022) published that microglial deletion of *Pkm2* in 5XFAD mice resulted in a reduction in amyloid pathology, as we are reporting here. Our data are mutually supportive, in that our phenotypes on AD pathology are very similar. In the study by Pan et al., the phenotype was attributed to a reduction in lactate production, which led to a reduction in lactyl modification in histone H4K12 and its transcriptional targets of inflammatory cytokines upon deleting *Pkm2* in microglia. They, however, observed a ~3-fold compensatory increase in PKM1 protein levels in microglia upon deleting PKM2, which we did not. The reason for the difference is not clear, but it may be due to the amount of tamoxifen administered; Pan et al. used 4 mg, while we used 1.5 mg of tamoxifen per mouse. Regardless of the reason, the question of interest is how much the observed increase in PKM1 contributed to overall lactate levels, since PKM1 is constitutively active with a greater activity than PKM2 (Christofk et al., 2008a,b).

In the nervous system, PKM2 expression was shown to increase under various pathological conditions in areas such as the retina, Schwann cells, and also in transcriptionally induced neurons (iNs) from iPSC (Zhang et al., 2015; Rajala et al., 2018; Babetto et al., 2020; Seki et al., 2020; Han et al., 2021; Traxler et al., 2022). These findings suggest that metabolic imbalance accompanies various neuropathological conditions and PKM2 and possibly HK2 (Hu et al., 2022) are likely to play important roles in shaping the outcome. Traxler et al. (2022) in particular illustrated that the effect of PKM2 was responsible for iNs to adopt aerobic glycolysis in culture, and attributed the metabolic effect to nuclear PKM2. It is highly likely that when PKM2 expression is dramatically upregulated, a portion of PKM2 translocates to the nucleus, although a majority of PKM2 appeared in the cytoplasm and processes as we have observed in microglia. Despite such a large increase in PKM2, probably as tetramers in microglial cytoplasm, it is plausible that the observed effect includes nuclear activation of PKM2. What regulates nuclear translocation of PKM2 is likely to depend on the affected cell types under neuropathological conditions.

We acknowledge that the findings from our study of PKM2 in microglia from 5XFAD mice are unlikely to be analogous to those of PKM2 in microglia from non-FAD background. Our results attest nonetheless to their own significance, since PKM2 exerts its impact on metabolism after its levels increase dramatically under pathological conditions. For instance, we have shown that deleting *Pkm2* in $CD4^+$ T cells had hardly any effect until the mice were subjected to EAE induction (Seki et al., 2020). Phenotypes from PKM2 activation with TEPP-46 was also observed only after perturbations of T-cell differentiation or demyelination injuries. These results are consistent with the fact that microglia undergo polarization only when they encounter external stimuli of both pro- and anti-inflammatory cytokines (Madore et al., 2020). In our study, the FAD phenotype was the stress stimuli.

Johnson et al. (2020) reported that PKM protein levels increase in the sugar metabolism module from AD cases compared to control subjects, although they did not make the distinction between PKM1 and PKM2. The sugar metabolism module was enriched with astrocytes and microglia, supporting our results. Surprisingly, the authors found that PKM protein is released into CSF along with LDHb, and the amount released correlated with disease progression, and with a decrease of amyloid β and an increase of tau/*p*-tau ratios in the CSF. This correlation may suggest that glucose homeostasis is also likely to contribute to tau pathology in human AD. In addition, since its increase in CSF is detected in asymptomatic cases, it may be possible to develop an assay for PKM2 as an early diagnostic for incipient AD.

References

Anastasiou D, et al. (2012) Pyruvate kinase M2 activators promote tetramer formation and suppress tumorigenesis. Nat Chem Biol 8:839–847.

Angiari S, et al. (2020) Pharmacological activation of pyruvate kinase M2 inhibits CD4(+) T cell pathogenicity and suppresses autoimmunity. Cell Metab 31:391–405 e398.

Babetto E, Wong KM, Beirowski B (2020) A glycolytic shift in Schwann cells supports injured axons. Nat Neurosci 23:1215–1228.

Baik SH, Kang S, Lee W, Choi H, Chung S, Kim JI, Mook-Jung I (2019) A breakdown in metabolic reprogramming causes microglia dysfunction in Alzheimer's disease. Cell Metab 30:493–507 e496.

Bellenguez C, et al. (2022) New insights into the genetic etiology of Alzheimer's disease and related dementias. Nat Genet 54:412–436.

Bonnet S, et al. (2007) A mitochondria-K+ channel axis is suppressed in cancer and its normalization promotes apoptosis and inhibits cancer growth. Cancer Cell 11:37–51.

Buescher JM, et al. (2015) A roadmap for interpreting (13)C metabolite labeling patterns from cells. Curr Opin Biotechnol 34:189–201.

Chen M, David CJ, Manley JL (2012) Concentration-dependent control of pyruvate kinase M mutually exclusive splicing by hnRNP proteins. Nat Struct Mol Biol 19:346–354.

Christofk HR, Vander Heiden MG, Harris MH, Ramanathan A, Gerszten RE, Wei R, Fleming MD, Schreiber SL, Cantley LC (2008b) The M2 splice isoform of pyruvate kinase is important for cancer metabolism and tumour growth. Nature 452:230–233.

Christofk HR, Vander Heiden MG, Wu N, Asara JM, Cantley LC (2008a) Pyruvate kinase M2 is a phosphotyrosine-binding protein. Nature 452:181–186.

Davalos D, Grutzendler J, Yang G, Kim JV, Zuo Y, Jung S, Littman DR, Dustin ML, Gan WB (2005) ATP mediates rapid microglial response to local brain injury in vivo. Nat Neurosci 8:752–758.

David CJ, Chen M, Assanah M, Canoll P, Manley JL (2010) HnRNP proteins controlled by c-Myc deregulate pyruvate kinase mRNA splicing in cancer. Nature 463:364–368.

Dayton TL, Jacks T, Vander Heiden MG (2016) PKM2, cancer metabolism, and the road ahead. EMBO Rep 17:1721–1730.

de Chaumont F, et al. (2012) Icy: an open bioimage informatics platform for extended reproducible research. Nat Methods 9:690–696.

Dzyubenko E, Rozenberg A, Hermann DM, Faissner A (2016) Colocalization of synapse marker proteins evaluated by STED-microscopy reveals patterns of neuronal synapse distribution in vitro. J Neurosci Methods 273:149–159.

Etienne F, Mastrolia V, Maroteaux L, Girault JA, Gervasi N, Roumier A (2019) Two-photon imaging of microglial processes' attraction toward ATP or serotonin in acute brain slices. J Vis Exp 143:e58788.

Gao X, Wang H, Yang JJ, Liu X, Liu ZR (2012) Pyruvate kinase M2 regulates gene transcription by acting as a protein kinase. Molecular Cell 45:598–609.

Geltink RIK, Kyle RL, Pearce EL (2018) Unraveling the complex interplay between T cell metabolism and function. Annu Rev Immunol 36:461–488.

Gu Z, Eils R, Schlesner M (2016) Complex heatmaps reveal patterns and correlations in multidimensional genomic data. Bioinformatics 32:2847–2849.

Han J, et al. (2021) Aberrant role of pyruvate kinase M2 in the regulation of gamma-secretase and memory deficits in Alzheimer's disease. Cell Rep 37:110102.

Hao Y, et al. (2021) Integrated analysis of multimodal single-cell data. Cell 184:3573–3587 e3529.
Harrington AW, Kim JY, Yoon SO (2002) Activation of Rac GTPase by p75 is necessary for c-jun N-terminal kinase-mediated apoptosis. J Neurosci 22: 156–166.
Hitosugi T, et al. (2009) Tyrosine phosphorylation inhibits PKM2 to promote the Warburg effect and tumor growth. Sci Signal 2:ra73.
Hu Y, et al. (2022) Dual roles of hexokinase 2 in shaping microglial function by gating glycolytic flux and mitochondrial activity. Nat Metab 4:1756–1774.
Huang Y, Happonen KE, Burrola PG, O'Connor C, Hah N, Huang L, Nimmerjahn A, Lemke G (2021) Microglia use TAM receptors to detect and engulf amyloid beta plaques. Nat Immunol 22:586–594.
Huang SC, Smith AM, Everts B, Colonna M, Pearce EL, Schilling JD, Pearce EJ (2016) Metabolic reprogramming mediated by the mTORC2-IRF4 signaling axis is essential for macrophage alternative activation. Immunity 45:817–830.
Israelsen WJ, et al. (2013) PKM2 isoform-specific deletion reveals a differential requirement for pyruvate kinase in tumor cells. Cell 155:397–409.
Jansen IE, et al. (2019) Genome-wide meta-analysis identifies new loci and functional pathways influencing Alzheimer's disease risk. Nat Genet 51: 404–413.
Jin S, Guerrero-Juarez CF, Zhang L, Chang I, Ramos R, Kuan CH, Myung P, Plikus MV, Nie Q (2021) Inference and analysis of cell-cell communication using CellChat. Nat Commun 12:1088.
Johnson ECB, et al. (2020) Large-scale proteomic analysis of Alzheimer's disease brain and cerebrospinal fluid reveals early changes in energy metabolism associated with microglia and astrocyte activation. Nat Med 26: 769–780.
Jung S, Aliberti J, Graemmel P, Sunshine MJ, Kreutzberg GW, Sher A, Littman DR (2000) Analysis of fractalkine receptor CX(3)CR1 function by targeted deletion and green fluorescent protein reporter gene insertion. Mol Cell Biol 20:4106–4114.
Kennedy AM, Frackowiak RS, Newman SK, Bloomfield PM, Seaward J, Roques P, Lewington G, Cunningham VJ, Rossor MN (1995) Deficits in cerebral glucose metabolism demonstrated by positron emission tomography in individuals at risk of familial Alzheimer's disease. Neurosci Lett 186:17–20.
Keren-Shaul H, et al. (2017) A unique microglia type associated with restricting development of Alzheimer's disease. Cell 169:1276–1290 e1217.
Kleinberger G, et al. (2017) The FTD-like syndrome causing TREM2 T66M mutation impairs microglia function, brain perfusion, and glucose metabolism. EMBO J 36:1837–1853.
Kramer A, Green J, Pollard J Jr, Tugendreich S (2014) Causal analysis approaches in Ingenuity Pathway Analysis. Bioinformatics 30: 523–530.
Kunkle BW, et al. (2019) Genetic meta-analysis of diagnosed Alzheimer's disease identifies new risk loci and implicates Aβ, tau, immunity and lipid processing. Nat Genet 51:414–430.
Lee JK, Tansey MG (2013) Microglia isolation from adult mouse brain. Methods Mol Biol 1041:17–23.
Li X, Zhou HP, Peng J, Li Q, Mei M (2023) Microglia PKM2 mediates neuroinflammation and neuron loss in mice epilepsy through the astrocyte C3-neuron C3R signaling pathway. Brain Sciences 13:262.
Lunt SY, et al. (2015) Pyruvate kinase isoform expression alters nucleotide synthesis to impact cell proliferation. Mol Cell 57:95–107.
Madore C, Yin Z, Leibowitz J, Butovsky O (2020) Microglia, lifestyle stress, and neurodegeneration. Immunity 52:222–240.
Marchetti P, Fovez Q, Germain N, Khamari R, Kluza J (2020) Mitochondrial spare respiratory capacity: mechanisms, regulation, and significance in non-transformed and cancer cells. FASEB J 34:13106–13124.
Mazurek S (2011) Pyruvate kinase type M2: a key regulator of the metabolic budget system in tumor cells. Int J Biochem Cell Biol 43:969–980.
Mills EL, et al. (2016) Succinate dehydrogenase supports metabolic repurposing of mitochondria to drive inflammatory macrophages. Cell 167:457–470 e413.
Niedenfuhr S, Wiechert W, Noh K (2015) How to measure metabolic fluxes: a taxonomic guide for (13)C fluxomics. Curr Opin Biotechnol 34:82–90.
Oakley H, et al. (2006) Intraneuronal beta-amyloid aggregates, neurodegeneration, and neuron loss in transgenic mice with five familial Alzheimer's disease mutations: potential factors in amyloid plaque formation. J Neurosci 26:10129–10140.
Palsson-McDermott EM, et al. (2015) Pyruvate kinase M2 regulates Hif-1alpha activity and IL-1beta induction and Is a critical determinant of the Warburg effect in LPS-activated macrophages. Cell Metab 21:347.
Pan RY, et al. (2022) Positive feedback regulation of microglial glucose metabolism by histone H4 lysine 12 lactylation in Alzheimer's disease. Cell Metab 34: 634–648.
Parhizkar S, et al. (2019) Loss of TREM2 function increases amyloid seeding but reduces plaque-associated ApoE. Nat Neurosci 22:191–204.
Parhizkar S, et al. (2023) Sleep deprivation exacerbates microglial reactivity and abeta deposition in a TREM2-dependent manner in mice. Sci Transl Med 15:eade6285.
Parkhurst CN, Yang G, Ninan I, Savas JN, Yates JR 3rd, Lafaille JJ, Hempstead BL, Littman DR, Gan WB (2013) Microglia promote learning-dependent synapse formation through brain-derived neurotrophic factor. Cell 155: 1596–1609.
Prakasam G, Singh RK, Iqbal MA, Saini SK, Tiku AB, Bamezai RNK (2017) Pyruvate kinase M knockdown-induced signaling via AMP-activated protein kinase promotes mitochondrial biogenesis, autophagy, and cancer cell survival. J Biol Chem 292:15561–15576.
Pucino V, et al. (2019) Lactate buildup at the site of chronic inflammation promotes disease by inducing CD4+ TCell metabolic rewiring. Cell Metabolism 30:1055–1074.
Rajala A, Wang Y, Soni K, Rajala RVS (2018) Pyruvate kinase M2 isoform deletion in cone photoreceptors results in age-related cone degeneration. Cell Death Dis 9:737.
Reiman EM, Caselli RJ, Yun LS, Chen K, Bandy D, Minoshima S, Thibodeau SN, Osborne D (1996) Preclinical evidence of Alzheimer's disease in persons homozygous for the epsilon 4 allele for apolipoprotein E. N Engl J Med 334:752–758.
Romero-Ramirez L, Garcia-Rama C, Wu S, Mey J (2022) Bile acids attenuate PKM2 pathway activation in proinflammatory microglia. Sci Rep 12: 1459.
Schwartzentruber J, et al. (2021) Genome-wide meta-analysis, fine-mapping and integrative prioritization implicate new Alzheimer's disease risk genes. Nat Genet 53:392–402.
Seki SM, et al. (2020) Modulation of PKM activity affects the differentiation of TH17 cells. Sci Signal 13:eaay9217.
Stanley M, Macauley SL, Holtzman DM (2016) Changes in insulin and insulin signaling in Alzheimer's disease: cause or consequence? J Exp Med 213: 1375–1385.
Tannahill GM, et al. (2013) Succinate is an inflammatory signal that induces IL-1beta through HIF-1alpha. Nature 496:238–242.
Traxler L, et al. (2022) Warburg-like metabolic transformation underlies neuronal degeneration in sporadic Alzheimer's disease. Cell Metab 34:1248–1263.e1246.
Ulland TK, et al. (2017) TREM2 maintains microglial metabolic fitness in Alzheimer's disease. Cell 170:649–663 e613.
Van den Bossche J, O'Neill LA, Menon D (2017) Macrophage immunometabolism: where Are We (going)? Trends Immunol 38:395–406.
Vander Heiden MG, et al. (2011) Metabolic pathway alterations that support cell proliferation. Cold Spring Harb Symp Quant Biol 76:325–334.
Vander Heiden MG, Cantley LC, Thompson CB (2009) Understanding the Warburg effect: the metabolic requirements of cell proliferation. Science 324:1029–1033.
Vats D, Mukundan L, Odegaard JI, Zhang L, Smith KL, Morel CR, Wagner RA, Greaves DR, Murray PJ, Chawla A (2006) Oxidative metabolism and PGC-1beta attenuate macrophage-mediated inflammation. Cell Metab 4:13–24.
Wang Y, et al. (2015) TREM2 lipid sensing sustains the microglial response in an Alzheimer's disease model. Cell 160:1061–1071.
Wang F, Zhang S, Vuckovic I, Jeon R, Lerman A, Folmes CD, Dzeja PP, Herrmann J (2018) Glycolytic stimulation Is Not a requirement for M2 macrophage differentiation. Cell Metab 28:463–475 e464.
Wculek SK, et al. (2023) Oxidative phosphorylation selectively orchestrates tissue macrophage homeostasis. Immunity 56:516–530 e519.
Weinberg SE, Sena LA, Chandel NS (2015) Mitochondria in the regulation of innate and adaptive immunity. Immunity 42:406–417.
Wick AN, Drury DR, Nakada HI, Wolfe JB (1957) Localization of the primary metabolic block produced by 2-deoxyglucose. J Biol Chem 224: 963–969.
Wightman DP, et al. (2021) A genome-wide association study with 1,126,563 individuals identifies new risk loci for Alzheimer's disease. Nat Genet 53: 1276–1282.

Xiang X, et al. (2021) Microglial activation states drive glucose uptake and FDG-PET alterations in neurodegenerative diseases. Sci Transl Med 13: eabe5640.

Yang W, Xia Y, Ji H, Zheng Y, Liang J, Huang W, Gao X, Aldape K, Lu Z (2011) Nuclear PKM2 regulates b-catenin transactivation upon EGFR activation. Nature 480:118–142.

Yao J, Irwin RW, Zhao L, Nilsen J, Hamilton RT, Brinton RD (2009) Mitochondrial bioenergetic deficit precedes Alzheimer's pathology in female mouse model of Alzheimer's disease. Proc Natl Acad Sci U S A 106:14670–14675.

Yoon SO, et al. (2012) JNK3 perpetuates metabolic stress induced by Abeta peptides. Neuron 75:824.

Zhang J, Feng G, Bao G, Xu G, Sun Y, Li W, Wang L, Chen J, Jin H, Cui Z (2015) Nuclear translocation of PKM2 modulates astrocyte proliferation via p27 and -catenin pathway after spinal cord injury. Cell Cycle 14:2609–2618.

Zheng GX, et al. (2017) Massively parallel digital transcriptional profiling of single cells. Nat Commun 8:14049.

Zhou Y, et al. (2020) Human and mouse single-nucleus transcriptomics reveal TREM2-dependent and TREM2-independent cellular responses in Alzheimer's disease. Nat Med 26:131–142.